UNIVERSIDADE D
COIMBRA

Jorge Miguel Caessa de Sousa

ON THE MECHANICAL AND TRIBOLOGICAL CHARACTERIZATION OF MoSeC COATINGS DEPOSITED BY SPUTTERING

Dissertação no âmbito do Mestrado Integrado em Engenharia Mecânica, ramo de Produção e Projeto, orientada pelo Professor Doutor Albano Augusto Cavaleiro Rodrigues de Carvalho e pelo Doutor Todor Vuchkov e apresentada ao Departamento de Engenharia Mecânica da Faculdade de Ciências e Tecnologia da Universidade de Coimbra.

Março de 2020

FACULDADE DE CIÊNCIAS E TECNOLOGIA
UNIVERSIDADE D COIMBRA

On the Mechanical and Tribological Characterization of MoSeC Coatings Deposited by Sputtering

Submitted in Partial Fulfilment of the Requirements for the Degree of Master's in Mechanical Engineering in the speciality of Production and Project

Author

Jorge Sousa

Advisor[s]

Professor Albano Cavaleiro

Doutor Todor Vuchkov

Jury

President	**Professor Doutor Marta Cristina Cardoso de Oliveira** **Professor Associado da Universidade de Coimbra**
Vowel[s]	**Professor Doutor Ana Sofia Figueira Ramos** **Professor Auxiliar da Universidade de Coimbra**
Advisor	**Professor Doutor Albano Augusto Cavaleiro Rodrigues de Carvalho** **Professor Catedrático da Universidade de Coimbra**

IPN – Instituto Pedro Nunes and UC – Universidade de Coimbra Collaboration

Instituto Pedro Nunes

Universidade de Coimbra

Coimbra, March, 2020

Two simple, yet powerful quotes, constitute the engine behind this thesis:

“If you cannot explain it to a six-year-old, you do not understand it yourself.”
Albert Einstein “

(Just keep it simple.)

“However difficult life may seem, there is always something you can do, and succeed at. It matters that you do not just give up.”
Stephen Hawking

(No matter the circumstances you are at, persevere.)

ACKNOWLEDGEMENTS

Before anything else, I want to thank Professor Albano Cavaleiro, the supervisor of this thesis. He made me feel welcome as I met every person, not only in Departamento de Engenharia Mecânica (DEM), but also in Instituto Pedro Nunes (IPN). As professor refers to himself, he was a facilitator, before, and during all my thesis, as he always provided me his precious time, and offered me guidance, from the first moment to the last.

Also, I want to write down a huge thanks to the industrially experienced, former PhD student, Nuno Parreira, as his regular presence, in person or not, helped me to keep motivated. With his assistance, I was able to rapidly possess a validation on my work structure and content, at times when the presential regime was not allowed.

Advice given by Todor Vuchkov and Talha Yaqub, two recent investigators, was also of fundamental importance. They were with me most of the time, in person, and allowed me to see, and, in any secure case, do, what was necessary to advance, experimentally, in my research. In every doubt I had, they were always available to clarify me.

Together with these four persons, I would like to express my gratitude to both IPN and UC institutions that permitted my presence in there, during my research, even in initial moments, when a virus started to torment the world. IPN and UC people did not raise any inconvenient, other than the need to guarantee the adequate fulfillment of the security procedures. In IPN, also, a special thanks to Ana Manaia must be given, as she was the first bridge, together with professor Albano, between me and the project I was going to work in.

Finally, I must extend this acknowledgment list to my parents and girlfriend. With their warming presence, I always felt supported. These are the most important people in my life and, in anything relevant that I do, these deserve to be the people I am always grateful to.

Abstract

A recent study suggests that about 20 % of the consumed energy worldwide is related to friction and 18 % of this energy could be saved. MoSeC coatings present a tremendous potential in domains where friction reduction is aimed like in the tool and automotive industries. They possess exquisitely low friction coefficients in diverse environments and can self-adapt to a variety of sliding conditions. In this investigation, a magnetron sputtering device, in direct current mode, is utilized to deposit MoSeC coatings with carbon content ranging between 6 and 60 at. % of C. Then, the carbon content influence on the final MoSeC film is analyzed by using different compositional (chemical), morphological, structural, mechanical and tribological characterization techniques. From WDS (wavelength dispersive spectroscopy), a decrease in the chalcogenide over transition metal (Se/Mo) ratio with an increasing carbon content of the films was found. SEM (scanning electron microscopy) and AFM (atomic force microscopy) detected a columnar cross-sectional growth with high porosity and roughness for the pure $MoSe_2$ films but less voids and a continuously more homogeneous and compact morphology for medium and high carbon content coatings. GIRXD (grazing incidence X-ray diffraction) patterns showed a higher degree of amorphization for increased carbon content coatings. Scratch test combined with Rockwell C Indentation showed the best adhesion strength for the 51 and 60 at. % C films. Nanoindentation permitted to confirm that the stiffness and hardness of the coatings increase almost proportionally to the carbon content of the films, except for the two highest carbon content films, for which these properties almost stagnate. From POD (pin-on-disk) experiments performed in humid air it was disclosed that NBR (nitrile rubber) countersurfaces sliding against MoSeC demonstrate higher friction values than the steel ones sliding against the same coating; the CoF (coefficient of friction) is higher at 25°C than at 200°C. The friction curves displayed a higher running-in period for NBR relative to steel as well as for higher carbon content films relative to low. With 3D optical profilometer very high wear rates were measured for the pure $MoSe_2$ film; no general friction-wear proportionality was observed with increasing carbon content, even though the augmented carbon content coatings exhibited less wear and elevated CoF. The lowest absolute specific wear rates were achieved for the 51 at. % of C film, which combines increased hardness, stiffness and compactness. It was also found that, for MoSeC films tested in humid air, at 200°C and against a steel surface, the wear track scar width

correlates better with the CoF than the specific wear rate. As summarized in a selection matrix, it was concluded that the coating with about 51 at. % of C displays the best combination of mechanical and tribological properties, followed by the 60 at. % of C.

Keywords MoSeC coatings, Self-lubricant coatings, Tribology, Magnetron Sputtering

Resumo

Um estudo recente sugere que cerca de 20 % da energia consumida mundialmente está relacionada com o atrito e 18 % dessa energia poderia ser economizada se fossem tomadas medidas convenientes. Os revestimentos MoSeC apresentam um enorme potencial em domínios onde é pretendida uma redução do atrito, como nas indústrias automotiva e de ferramentas. Estes revestimentos possuem coeficientes de atrito excecionalmente baixos em diversos ambientes e podem se auto adaptar a uma variedade de condições de deslizamento. Nesta investigação, é utilizado um equipamento de pulverização catódica magnetrão, em modo de corrente contínua, para depositar revestimentos MoSeC com teor de carbono variando entre 6 e 60 % at. em C. Em seguida, é analisada a influência do conteúdo de carbono no filme MoSeC através de inúmeras técnicas de caracterização composicional (química), morfológica, estrutural, mecânica e tribológica. A partir de WDS (espectroscopia dispersiva de comprimento de onda), foi encontrada uma diminuição na razão calcogeneto sobre metal de transição (Se/Mo) com o aumento no teor de carbono dos filmes. SEM (microscopia eletrónica de varrimento) e AFM (microscopia de força atómica) permitiram detetar um crescimento colunar com alta porosidade e rugosidade para os filmes de $MoSe_2$ puro, mas menos poros e uma morfologia progressivamente mais homogénea e compacta para revestimentos de médio e alto teor de carbono. Os padrões de GIRXD (difração de raios-X de incidência rasante) mostraram um maior grau de amorfização para revestimentos com maior teor de carbono. O teste de indentação deslizante combinado com indentação Rockwell C mostraram a ocorrência da melhor adesão para os filmes de 51 e 60 % at. em C. A técnica de nanoindentação confirmou que a rigidez e dureza dos revestimentos aumentam quase proporcionalmente ao teor de carbono dos filmes, exceto para os dois filmes de maior teor de carbono, nos quais essas propriedades quase estagnam. A partir de testes POD (pino no disco) realizados em ar húmido, foi mostrado que as superfícies NBR (borracha nitrílica) deslizando contra MoSeC têm valores de atrito mais altos do que as superfícies de aço deslizando contra o mesmo revestimento, e que o CoF é maior a 25°C do que a 200°C. As curvas de atrito exibiram períodos de "running-in" mais longos para NBR do que para aço; do mesmo modo, estes períodos são mais longos para teores de carbono mais elevados. Com o perfilómetro ótico 3D foram medidas taxas de desgaste muito altas para o filme $MoSe_2$ puro, não tendo sido verificada qualquer

proporcionalidade geral entre desgaste e atrito com o aumento do teor de carbono, embora os revestimentos com maior teor de carbono exibam menor desgaste e CoF mais elevado. As menores taxas de desgaste específico absoluto foram alcançadas para o revestimento com 51 % at. em C, que combina maior dureza, rigidez e compacidade. Também foi descoberto que, para filmes MoSeC testados em ar húmido, a 200 ° C e contra uma superfície de aço, a largura da pista de desgaste se correlaciona melhor com o CoF do que a taxa de desgaste específica. Conforme resumido numa matriz de seleção, concluiu-se que o revestimento com cerca de 51 % at. em C exibe a melhor combinação de propriedades mecânicas e tribológicas.

Palavras-chave: Revestimentos MoSeC, Revestimentos Autolubrificantes, Tribologia, Pulverização Catódica Magnetrão

Contents

LIST OF FIGURES

LIST OF TABLES

LIST OF ABBREVIATIONS

AISI – American Iron and Steel Institute

AFM – Atomic Force Microscopy

CoF – Coefficient of Friction

CVD – Chemical Vapor Deposition

DC – Direct Current

DEM – Departamento de Engenharia Mecânica

DLC – Diamond Like Carbon

EFTEM – Energy Filtered Transmission Electron Microscopy

FCTUC – Faculdade de Ciências e Tecnologia da Universidade de Coimbra

GIXRD – Grazing Incidence X-ray Diffraction

HER – Hydrogen Evolution Reaction

NBR – Nitrile Rubber

PVD – Physical Vapor Deposition

RF – Radio Frequency

SEM – Scanning Electron Microscopy

TEM – Transmission Electron Microscopy

TMD – Transition Metal Dichalcogenides

TMD-C – TMD with Carbon

XRD – X-ray Diffraction

WDS – Wavelength Dispersive Spectroscopy

1. INTRODUCTION

"I start where the last man left off". This quote, by Thomas Edison, describes precisely what the scientific research is about. Nothing can be accomplished without help from previous work developments. The present thesis does not shift the paradigm.

Several things are already known about the MoSeC film. First, that it is constituted by $MoSe_2$ self-adaptive nanoparticles immersed in an amorphous carbon phase. Also, despite having only few microns of thickness, the MoSeC coating has potential to be a solid lubricant, presents beneficial electrical and optical properties and, specially, shows advanced mechano-tribological properties [1, 2, 3]. Some properties of this coating that reveal paramount importance include high hardness and compactness (compared to pure sputtered TMD coatings), elevated frictional stability, with exquisitely low friction coefficients in varied environments (dry nitrogen, humid air and vacuum), and enhanced wear and oxidation resistances compared to similar coatings. The MoSeC coating can also display a chameleon effect, as it is capable to self-adapt for a variety of sliding conditions as long as the sliding occurs in a direction parallel to the film crystallographic basal planes orientation [3].

Although many characteristics of the coating are familiar, some remain uncertain. Until now, MoSeC coatings deposited via an unbalanced magnetron sputtering device are not present in many studies. Thus, if there exists an ideal equilibrium on the carbon and $MoSe_2$ chemical compositions which provide the best friction behaviors and mechanical properties, right now, it is still doubtful. If a higher carbon content, up to a certain threshold, is achieved in the coating, it usually provides higher compactness and hardness of the coatings, which are needed mechanically and tribologically [4]. On the other hand, a higher carbon content tendentially translates in a decreased content of the $MoSe_2$ self-lubricant phase, necessary for tribological behavior [5].

Thus, briefly, in this work, one of the major incremental advances in the field of solid lubricants attempted is a clarification on the optimized MoSeC coating chemical composition to provide the lowest friction and wear, while maintaining a self-adaptive mechanism to the sliding conditions and beneficial mechanical and tribological properties. This advance is achieved via depositing MoSeC coatings with several contents of carbon (6 at. % of C, 24 at. % of C, 33 at. % of C, 51 at. % of C and 60 at. % of C), by varying the currents applied to each carbon target, in an unbalanced magnetron sputtering deposition device, in order to test the influence of a carbon

variation on the final coating microstructure and properties. The rating of the different carbon content coatings is then checked via a set of available characterization techniques, some of which are yet to be performed in MoSeC coatings. For example, the first ever CoF outcomes for MoSeC surfaces sliding against rubber (NBR) are checked via pin-on-disk characterization technique.

One poorly solved research gap of the current literature is thus targeted through this study. But why should this gap be filled? Where can MoSeC be applied? There is a variety of situations where liquid lubricants are not desired. This occurs in optical systems or in some electronics [6]. Also, because of the environmental and economic impact of liquid lubricants, another lubrication mechanism must emerge in aerospace, automotive and tool or manufacturing industries [5]. As lubricants fundamental concept is to limit energy loss, solid lubrication can too, reduce friction, thus providing a way to decrease energy demands. Consequently, the MoSeC film can replace liquid lubrication whilst enabling the use of renewed lightweight, cheap or less wear resistant bulk materials than the currently utilized, in a variety of areas, with consequent billion euros of worldwide market gains [6].

A thin MoSeC film, with only few nanometers of thickness, can have a significantly positive effect on the efficiency of the polymers molding process, e.g. tires molding. During the tires molding procedure, and when the tire is being released from the mold, a huge amount of rubber is lost at the expense of friction and adhesion phenomena in the contact areas. In the referred procedure, it is arduous to release the mold, hence, some common troubles on the rubber parts are usually found, named mold release defects. Also, when some adherent extra rubber sticks on the surface of the tire, after mold release, there is a mold fouling issue. Mold release and mold fouling root worse quality parts, higher costs and superior time spent in manufacturing. Despite already existing a solution to solve the tire molding problems, in the form of chemical release agents, that solution is not permanent [6, 7, 8]. Hence, the deposition of a MoSeC film on the mold surface, which diminishes adhesion between mold surface and rubber as it provides more similar surface energies between both surfaces, should provide a longer-lasting lubricating effect, and much higher effectiveness, as it avoids all the time currently spent to lubricate the sliding regions, in the molding process [7, 8, 9]. In conclusion, MoSeC may be a perfect fit, economically, environmentally and performance-wise, in the polymer molding market, whose worth was estimated as more than 11 billion euros in the year of 2017. [10]

Throughout this manuscript, an effort is made to maintain a logical order in the presentation of each chapter. Thus, after the introduction, in Chapter 2, the author explains a real existing industrial problem originated in friction and wear mechanisms, and the way the MoSeC

coating can present a longer-lasting solution to it, than liquid lubricants. In the following chapter, some questions about the developed coating are answered. The chemical composition, structure, properties and growth of the films are approached. This chapter is structured as a funnel. The explanation starts with the basics of what is a coating, progresses with solid lubricants and TMDs (transition metal dichalcogenides) concepts, and finally, provides details on the nanocomposite deposited in this work, such as the MoSeC specific properties and its edges over the competition, like its self-adaptive behavior and exquisitely low friction coefficient in a variety of environments. Chapter 4 refers to some basic aspects of thin films and explains some of the thin film deposition methods and growth variations. In sequence, for Chapter 5 and the following, the experimental method is discussed, since the pre-deposition stage to the mechanical and tribological characterization of the final MoSeC coating. This chapter involves the pre-deposition method, the deposition process, and a very brief and synthetic introduction to all the characterization techniques carried and the equipment and parameters utilized in each of these techniques. Chapter 6 is the penultimate chapter. It displays all the major results extracted from each characterization technique and performs a comparison between all the distinct carbon content coatings for that single technique. Compositional characterization techniques such as WDS and SEM, morphological like AFM, structural as GIXRD (grazing incidence X-ray diffraction) and mechanical such as scratch, Rockwell C indentation and nanoindentation are carried out. Tribological characterization techniques like POD with NBR and DIN 100Cr6 bearing steel balls sliding against the MoSeC coating, at room temperature and at 200°C, for all carbon contents, with two repetitions for each test, were also performed, whilst the wear rate was assessed, for all POD tests, through the aid of a 3D optical profilometer.

2. INDUSTRIAL NEED

2.1. Industrial Problem

Quite often, polymers are manufactured by molding. This is the case for tires, generally processed in a complex procedure that involves several stages. One of these stages, curing, is when the actual molding process occurs, giving the tire its final shape. Curing is the process which involves applying pressure to the green tire (tire with all components finished and assembled, but not the final shape), through an expanding bladder inserted in its center, and an upper press that forces the tire against a lower mold [11].

The curing stage configuration is shown in **Figure 2.1**.

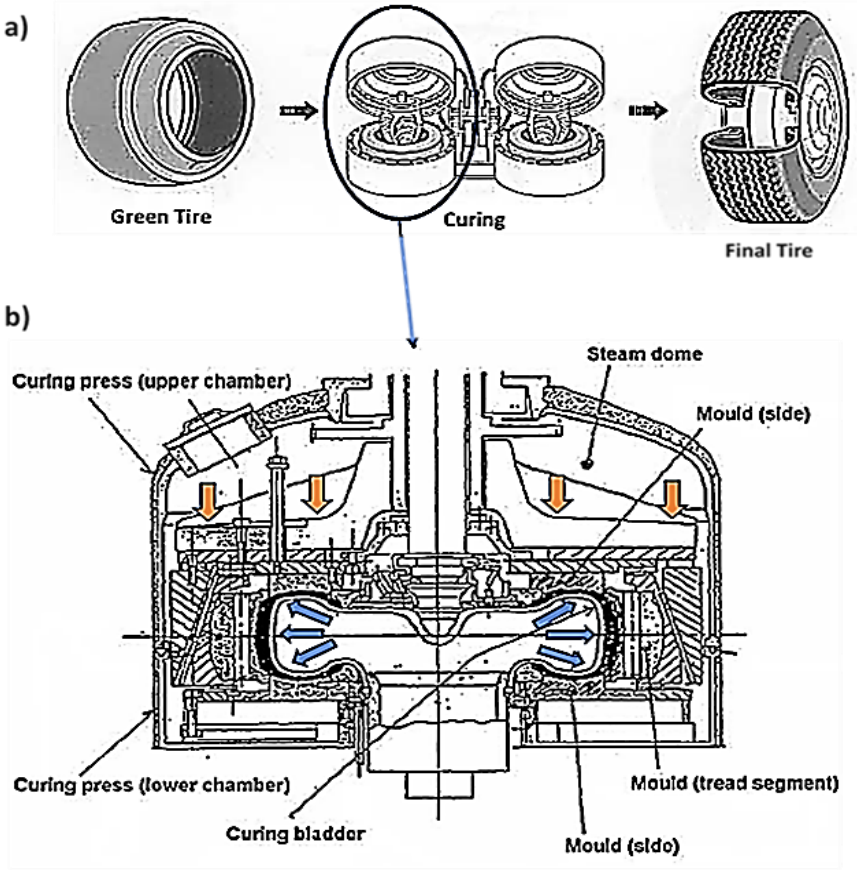

Figure 2.1. Tire curing process: a) aim, with the green tire being transformed into final tire, and b) detailed scheme presenting the configuration of the process and the forces involved – adapted from [11, 12].

In the end of the curing process, the upper curing press is lifted, and, the mold is released. Two molding problems can usually be observed throughout this step: i) mold release and ii) mold fouling [6]. The first is a difficulty in releasing the mold. The second, manifests as an accumulation of waste on the mold surface. Both troubles are related and can lead to defects such as those observed in **Figure 2.2**.

Figure 2.2. Tire molding defects due to: (left side) mold release; (right side) mold fouling – adapted from [13, 14].

2.2. Problem Causes

Why do these troubles appear? Since a tire is made of rubber, both the mentioned defects are related to the tribological behavior of this material. Therefore, because the fundamental aim of a solution to these problems is to attain a reduced shear force during mold release, friction and wear must be studied. Friction may be defined as the resistive load acting between two bodies in relative motion. Wear, on the other hand, is a tribological process referring to the damage caused in a solid surface. Generally, it involves the continuous removal of material from its original position on the surface, due to the relative motion between that surface and another substance [15]. The two are represented in **Figure 2.3**.

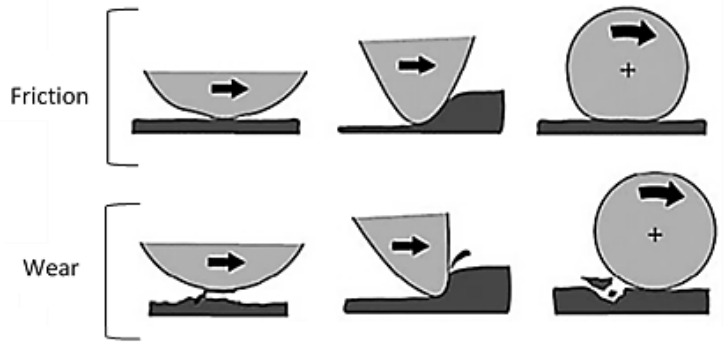

Figure 2.3. Schematics of the friction and wear components of tribology – adapted from [16].

Rubber friction has two major contributions: hysteretic and adhesive [17, 18]. The hysteretic is related to the indentation process during sliding between a rough substrate and rubber, which leads surface asperities of the rough substrate to exert oscillating forces on the rubber surface, causing its periodic deformation and energy dissipation, via internal damping [19]. Hysteresis decreases with a temperature increase. The adhesive contribution, on the other hand, is different. It occurs especially at lower loads, on very clean and smooth rubber surfaces and involves successive formation and breakage of contact patches, distributed over the nominal contact area. The adhesive component decreases when the normal pressure is enhanced [17, 19]. **Figure 2.4** represents both components of rubber friction.

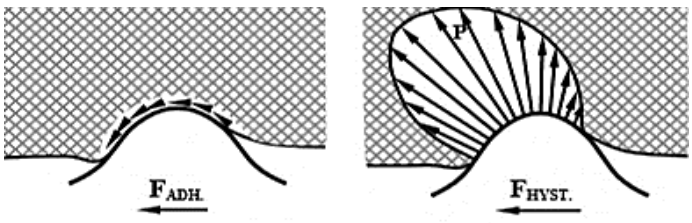

Figure 2.4. Adhesive (left) and hysteretic (right) force components in rubber friction – adapted from [17].

Due to the low pressures involved in the tires molding process, the adhesive component is probably the most relevant rubber friction component. It is originated by London-van der Waals intermolecular forces which attract rubber and metallic mold together, whenever the potential energy of the pair is negative. This premise is always valid, if the materials have a roughness which leads the distance between them to be higher than some Å [20, 21, 22, 23]. Owing to these attractive forces, the rubber surface becomes well-matched with the mold surface. Then, a phenomenon called wetting promotes even higher intermolecular attractions between both, and

if the surface energy of rubber is lower than the surface energy of the mold (γ rubber < γ mold), which is the case for a metallic mold, then rubber builds an area of itself in the mold, and adhesion is promoted [7, 8, 9].

Rubber wear occurs due to three different mechanisms: abrasion, fatigue and roll formation, but thanks to the rather low shear stress involved in the tires molding process, there, it takes place, mainly, due to abrasion and fatigue. Abrasive wear happens when tearing (local mechanical rupture) of the sliding surface of the elastomer takes place, during sliding against a countersurface with sharp texture whilst fatigue wear occurs on the surface of an elastomer that is sliding against blunt projections on the countersurface [17].

2.3. Current Solution and Potential Improvement

Current solutions to reduce the tires molding defects are chemical release agents. These are liquid-based solutions which can be applied to the tire, prior to curing, so that they aid the process of removing the tire from the mold. However, a release agent is not capable of a long-lasting effect and must be introduced several times in order to ensure contaminant-free releases and defect-free parts. This causes limitations on the production rate and significant costs to the industry [6, 7, 8, 9].

Solid lubricants can be explored as an answer for mold fouling and mold release defects, as they lead to much longer times between replacement than liquid lubricants, while maintaining very good quality in the tire sliding interface, with reduced defects [24]. Further, the solid lubricant decreases the CoF, as the presence of a TMD layer between rubber and the hard substrate lessens the surface energy of the substrate, and hence, reduces wetting and resultant adhesion [9].

Therefore, the solution proposed by this study in order to reduce mold sticking and rubber wastage, is to deposit a low friction, low wear solid lubricant film on the metallic mold, which presents lower surface energy than the current metallic mold (γ MoSeC ~ 40 mJ/m², γ mold ~ 60 mJ/m², for typical metallic molds), and a similar surface energy to the one found in rubber (γ rubber ~ 20 mJ/m²), together with increased hardness and compactness, that hinder the wear. This thin film, when applied to the mold, should diminish mold sticking, due to reduced wetting and adhesion, and should facilitate mold release, as it presents very low CoF.

The referred film is constituted by a carbon matrix coating, with self-adaptive layers of $MoSe_2$ and is the investigated solution to replace liquid lubricants in the tires molding process.

3. DEVELOPED COATING

The previously discussed tires molding industrial problem revealed a concrete example where liquid lubrication is not an optimal solution. As a result, solid lubricants are expected to provide a renewed ability to face the current tribological limitations. But several questions remain unanswered. What is the structure of these coatings? What properties do they have? How do they grow? How does the self-adaption process occur? All these, together with another huge amount of fundamental answers, still lack. So, in order to answer all these questions, a funnel approach is taken throughout the present chapter. This analogy means that the explanation starts with some basics, of what is a coating, progresses with some fundamental concepts such as solid lubricants and TMDs, and finally details the self-adaptive nanocomposites deposited in this work.

The word coating is a synonym for a material or chemical element added on another material, named as the substrate. A coating-substrate pair is illustrated in **Figure 3.1**.

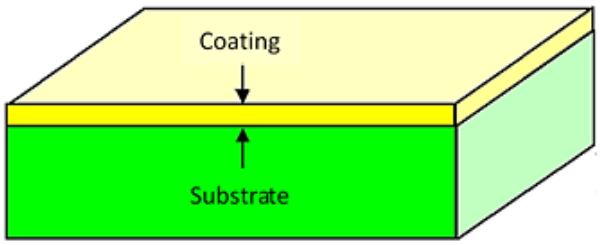

Figure 3.1. Representation of a coating-substrate pair – adapted from [25].

Forming a coating involves three distinct, although not always separate, stages. The first one is the production of species to be deposited. Then, these species are transported to the substrate. Finally, deposition is fomented, permitting the growth of a film. As this last step happens, a surface treatment occurs [26]. Numerous coatings can be produced with distinct material combinations, and choosing one among them, or developing a coating to a specific application, becomes challenging [2].

3.1. Solid Lubricant Coatings

Solid lubricant coatings came to discussion in the scientific community as a solution to replace conventional lubrication, but despite being under research for the past few decades, many attainable solid lubricant systems remain poorly explored [27]. Solid lubricants disclose themselves as promising candidates for applications where liquid lubrication is not desired or possible, such as in aerospace and automotive industries, in optical and electronic systems and in tool manufacturing [5]. Even in other general applications, these coatings proffer several advantages over liquid lubricants, such as superior thermal and oxidation stability at high temperature, or also, lower volatility. Therefore, if utilized properly, they can provide a competitive edge over liquid lubricants [27].

Various systems of solid lubricants were developed so far. Some involve: i) soft metals like Ag or Au, ii) metal oxides such as MoO_3 or PbO, iii) DLCs (diamond like carbon), iv) TMDs like MoS_2, $MoSe_2$, WS_2 or WSe_2 and v) WC/C (tungsten carbide with carbon). TMDs are, arguably, the ones with highest tribological potential, as they can afford extremely low CoF in dry nitrogen and vacuum, which even extends to humid air, for $MoSe_2$. Therefore, they have been combined with different materials, such as metals (e.g. Ti, Au, Pb or Zr), non-metals (e.g. C or N) and compounds (e.g. ZnO), to enhance their mechanical and structural properties [3, 5]. In this research, TMDs have been combined with carbon.

3.2. TMDs

TMDs constitute one kind of 2D materials that became interesting research-wise because they promote exquisitely low CoF in varied environments, along with a self-lubricating behavior. Some branches of science where they are vastly explored and show clear potential are in aerospace, catalysts, fuel cells, or even in solar energy converters [6].

3.2.1. TMDs Structure

TMDs belong to MX_2 series, where M is a transition metal and X = S, Se or Te. They exhibit a “sandwich” type of structure (X-M-X) in which metal atoms (M) are located in between two layers of chalcogen (X) **Figure 3.2** [28].

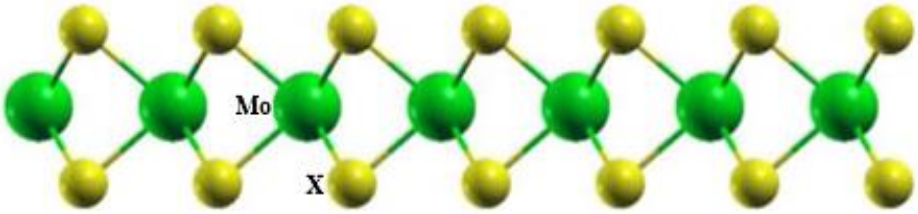

Figure 3.2. Side view of the common MoX_2 TMDs – adapted from [28].

Atoms within these three layers are bonded covalently, while individual sheets ("sandwiches") are connected by weak van der Walls interactions [29]. Its these weak interactions between adjacent molecular sheets that provide very low shear strengths and low friction between lamellae of the TMD **Figure 3.3** [30].

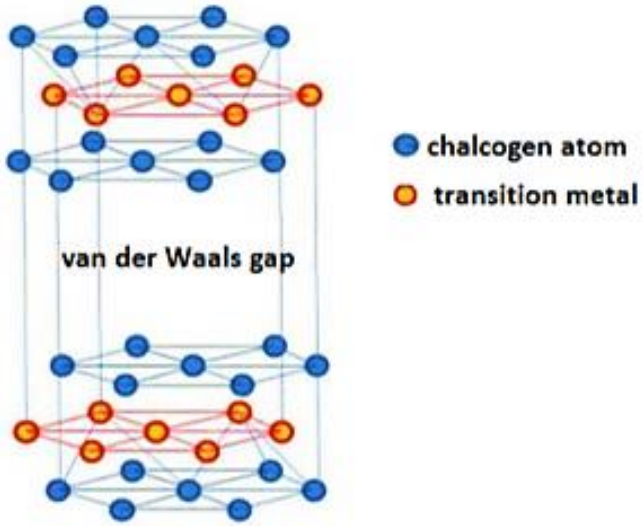

Figure 3.3. Structure of atomic layers of TMDs – adapted from [6].

When sliding of two surfaces in contact takes place in a plane parallel to the TMD layers, due to the weakness of the van der Waals forces that bring each sandwich of $MoSe_2$ together, the friction force exerted between surfaces is enough to adjust the TMD layers, which thereby move relative to one another and favor low friction sliding. Thus, the TMD phase reorients when exposed in a tribological contact, phenomenon which is ever more arduous whenever the TMD basal planes are oriented increasingly perpendicular to the sliding direction [6].

3.2.2. TMDs Properties

3.2.2.1. Friction

In the last topic, it was answered how friction is achieved in TMDs. However, some properties of TMDs related to friction must be additionally debated.

If sliding under ideal conditions, TMDs can be “frictionless” with CoF values as low as 0.001, which result from a synergetic effect between the sliding TMD tribolayer and the typical environmental conditions [31]. For most TMDs, these kinds of values are limited to vacuum or dry atmospheres, not only due to rapid oxidation outside these environments, but also because of the detrimental effect of water vapor in friction [30]. Nonetheless, for $MoSe_2$, humid air is also a favorable environment for the occurrence of sliding friction [32].

3.2.2.2. Hardness and Load-Bearing Capacity

One of the most successful ways for improving the tribological behavior of TMD coatings is to deposit them in a high strength matrix, forming a nanocomposite [32, 33].

But why composites? TMDs do not present high strength? The answer is no. Pure TMDs demonstrate low load-bearing capacity and hardness, attributed to a very porous structure, even when compared to other low-friction coatings, such as DLCs [34, 30].

These drawbacks make pure TMDs inappropriate for most applications submitted to high contact loads [3]. However, the hardness of TMDs can be significantly increased by doping them with a third element or even embedding them in a third element. This may mean doping or embedding TMD films in metals like Ti or Cr, prone to oxidation, or non-metals as N or C, whose tendency of oxide formation is a non-problematic issue since their oxides are gaseous and escape the contact without affecting the TMD coating. Non-metal dopants, such as carbon, which is utilized in this paper, have the advantage of allowing improved microstructures and mechanical properties without compromising friction performance [34].

3.2.2.3. Adhesion to the Substrate

Pure TMDs exhibit poor adhesion to the substrate, commonly peeling-off [34]. However, for a coating to be effective, it must not peel-off from the substrate at which it is applied and, therefore, good film-substrate adhesion is necessary. Due to the embedment of the TMD in an amorphous carbon matrix better adhesion is promoted. Furthermore, an adequate film-substrate adhesion may be promoted by several factors. Some comprise: i) achieving low

porosities, of both coating and substrate, to allow increased number of bonds at the interface; ii) strong atom-atom bonding at the interface; and; iii) reduced presence of oxide films and surface contaminants [6]. All these reasons are considered in this work, and the solution for the problem of poor adhesion to the substrate is surpassed by two fundamental motives: via deposition of a thin Cr (Chromium) interlayer between the M2 steel substrate and the MoSeC coating, followed by the deposition of a gradient layer with chemical composition between those of the substrate and the coating, so that the chemical composition transition is smoother; through controlling the deposition and cleaning parameters during the magnetron sputtering process so that the porosity and oxides are not prejudicial.

3.2.3. TMDs Orientation and Growth

Crystalline coatings are often divided according to the orientation of their basal planes. Briefly, type I orientation has perpendicular basal planes to the coating surface whereas type II orientation presents the basal planes parallel to the surface. Type I orientation is also mentioned by the Miller index (100), as basal (100) preferential orientation, and results in coatings that are highly porous and display worse shear properties. Type II, on the other hand, also referred as basal (002) preferential orientation, results in low shear strength planes that are parallel to the substrate surface, thus lessening the detachment of the film from the interlayer besides decreasing the force required to slide. Not surprisingly, the tribological response was evidenced as being more stable for higher ratios of (002)/(100) oriented basal planes, so type II orientation is needed to ensure friction reduction [1, 34].

3.3. TMD-C Nanocomposite

Nanocomposite is a multiphase solid material where one of the phases has at least one dimension with less than 100 nm [35]. It usually refers to a solid combination of a bulk matrix with nano-dimensional phases. The rationale which explains the use of a nanocomposite is that it allows to combine distinct properties from each of its constituents.

In this work, the nanocomposite coating is composed of a carbon matrix filled with TMD nanoparticles, hence the abbreviature TMD-C **Figure 3.4**. Its mechanical and tribological properties, combined with the possibility to have self-lubricating phases embedded in an amorphous matrix, gave rise to the self-adaptive nanocomposites concept.

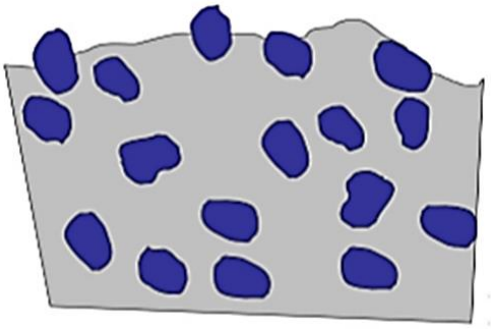

Figure 3.4. $MoSe_2$ nanoparticles embedded in a C-matrix – adapted from [36].

But what exactly is a self-lubricant? The aim of self-adaptive nanocomposites, also called "Chameleon Nanocomposites" is to adapt by themselves to the stresses and/or environmental conditions (atmosphere, contact stresses, thermal cycling and so forth) undergone by the contact. This may be achieved via formation of a thin film at the sliding interface, whenever the material is exposed to a shear load, as shown in **Figure 3.5** [2, 30, 37].

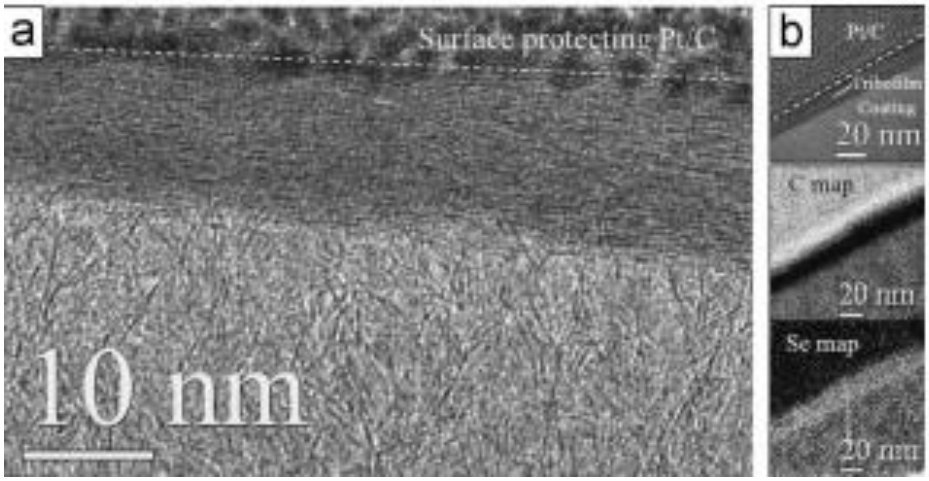

Figure 3.5. a) TEM (transmission electron microscopy) cut normal to the sliding direction from a MoSeC61C coating tribologically tested in humid air at 10 N. A neat structural modification happened at small depths (up to 20 nm); b) TEM of the same area and EFTEM (energy filtered transmission electron microscopy) maps of the same film area reveal the carbon absence and Se enrichment, confirming the formation and reorientation of $MoSe_2$ planes parallel to the sliding surface – adapted from [30].

3.3.1. MoSeC Nanocomposite

MoSeC is a TMD-C coating that has relatively low research volume, although it constitutes a potential candidate as a solid lubricant [38]. In the next paragraphs, the choice of $MoSe_2$ as the utilized TMD is explained due to its rich combination of electronic, optical and, majorly, mechano-tribological properties [39]. A short summary is also presented in **Table A.1**.

Electronically and optically, $MoSe_2$ is a semiconductor whose band gap is narrower than the one of the most utilized TMD, MoS_2 [40]. Hence, this semiconductor more probably displays an electrically conductive behavior rather than insulating, when submitted to a difference in potential. $MoSe_2$ band gap is direct for less than 1 % compressive strain [29]. Therefore, it presents good light absorption, important for photovoltaic applications. $MoSe_2$ shows, too, ultra-high activity as the HER (hydrogen evolution reaction) electro catalysts and the presence of Mo-C chemical bonds facilitate fast charge transfers [40, 41].

Mechanically, $MoSe_2$ is a ductile material, that sustains high deformations before fracture. It is elastically anisotropic and satisfies Born criteria, so it is stable [40]. Furthermore, although it exhibits a relatively poor oxidation resistance due to a low activation energy, it only triggers oxidation at higher temperatures than MoS_2, matching the same rates of oxidation just for 450°C. Besides all mechanical advantages mentioned, doping a substrate with MoSeC is suggested to foment favorable tribological results at temperatures up to 300°C in vacuum, dry and humid environments [30]. As compared to several TMDs, this coating exhibits higher ratio of chalcogen atoms over transition metal atoms (Se/Mo ratio, which can affect the crystallinity) and decreased shear modulus, which adds a positive impact for shearing whenever parallel orientation between the sliding direction and the coatings basal planes is achieved. Easy shearing further increases as $MoSe_2$ presents larger interplanar distances than other TMDs, which reduce van der Waals forces between basal planes [5].

But why join a carbon matrix to the $MoSe_2$? Studies on doping TMDs with carbon began in the late 90s with an idea of nanocomposite structured coatings that would combine nanocrystals of self-lubricant WS_2 (another compound in the family of TMDs) and hard WC phases embedded in an amorphous carbon matrix [6]. Cavaleiro et al. [42] presented an alike concept for WS_2 coatings doped with C or N. Such films showed a huge improvement of hardness and wear resistance compared to that of the un-doped coating. The carbon matrix contributes to improved hardness of the coatings with better protection against oxidation, as higher compactness of C-doped coatings promotes an increase to their environmental resistance [32]. It could be thought that just like carbon foments an enhanced hardness, it should also cause increased shear strength and, possibly,

friction. Despite, it was proven that the $MoSe_2$ is the phase which tendentiously dominates the sliding interface because it appears proportional to the local contact pressure, which is typically higher in the center of the wear track [30]. So, carbon is only found on the periphery of the friction track and hidden below the TMD, and the hypothesized effect is generally avoided. Thus, carbon does not usually lead to a significant increase in friction, and very likely it is preferentially removed from the sliding interface. A brief recap of the carbon choice is made in **Table A.2**.

3.3.1.1. MoSeC Behavior to Friction and Wear

MoSeC nanocomposite brings an improvement to tribology since, in the first place, i) it is a self-adaptive coating, which is capable of adaption to the stresses suffered during the sliding contact, and, in the second place, but not less important, ii) it provides a very low CoF in a varied number of environments. The self-adaptive behavior happens due to the free movement of adjacent sheets of the TMD, as the $MoSe_2$ platelets reorient parallel the sliding direction (as shown in **Figure 3.5**). The observed friction decrease, roots on the highly anisotropic crystal structure of TMDs, which connects basal planes through weak inter lamellae van der Waals forces (as illustrated in **Figure 3.3**). Generally, in MoSeC systems, not only the coatings display low friction, they also reveal decreased wear. Hence, MoSeC facilitates both improved wear resistance and low friction compared to other coatings.

In the next chapter, basic aspects of thin films and their growth are approached, together with explanations about the utilized film deposition process, unbalanced magnetron sputtering.

4. COATING DEPOSITION

4.1. Thin Films Basics and Growth

Thin films are a well-established technology in material science. Indeed, since the 1960s, a diversity of functional nanocoatings has been generated, which was possible due to improved abilities in the deployment of new thin film processing techniques, and in the control of distinct deposition parameters [43, 44]. Consequently, thin films began to possess novel properties that could not be found in bulk materials, such as multilayer aspects, which forced them to expand into a trend [43].

A thin film consists in a layer of material with thicknesses differing from several μm down to few nm. Hence, thin film technologies involve the deposition of one-by-one target molecules, atoms or ions, on a substrate. Indeed, a film with a thickness deviated from the mentioned range could provide diminished mechanical properties together with a worse frictional behavior [45]. For thinner coatings, asperities could break through the film and lead to the contact of the surfaces, thus increasing friction. On the other hand, for thicker coatings, adhesive failure would quickly be experienced, and result in the removal of large film segments, ultimately promoting a friction increase [46].

When a thin film is deposited on a substrate, it can grow in numerous ways. The three fundamental modes are: i) layer-by-layer mode, when film atoms are bound more strongly to the substrate than to each other. As a result, the 2D film is added and covers the substrate uniformly; ii) island mode, also named as columnar growth, when film atoms are more strongly bonded to each other than to the substrate, resulting in 3D islands that nucleate and grow directly on the substrate surface; iii) layer-plus-island mode which is an intermediate case between island and layer growth and represents the situation when after the growth of 2D layers, the growth of 3D islands takes place **Figure 4.1** [47].

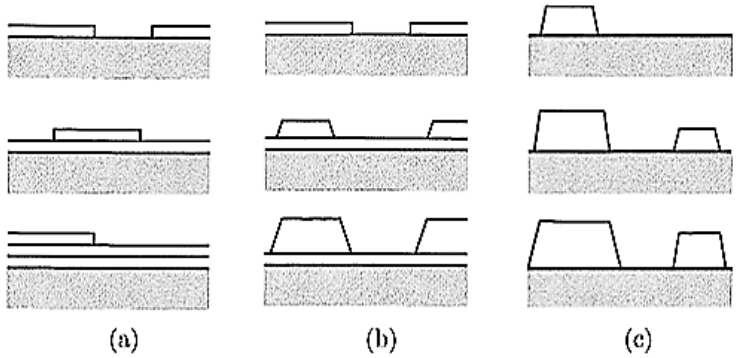

Figure 4.1. Schematics of thin films different growth modes: (a) layer-by-layer; (b) layer + islands; (c) islands – adapted from [47].

Layer-by-layer is the aimed growth mode, as it provides the most tribologically and mechanically stable coatings. As for the island mode, it usually originates porous films, with columnar structures growth. It is the typical mode for pure TMD coatings.

4.2. Deposition Methods

To form coatings, many deposition methods exist. The thin film deposition process divides in two major systems, referred as CVD (chemical vapor deposition) and PVD (physical vapor deposition). CVD and PVD are illustrated in **Figure 4.2** [6].

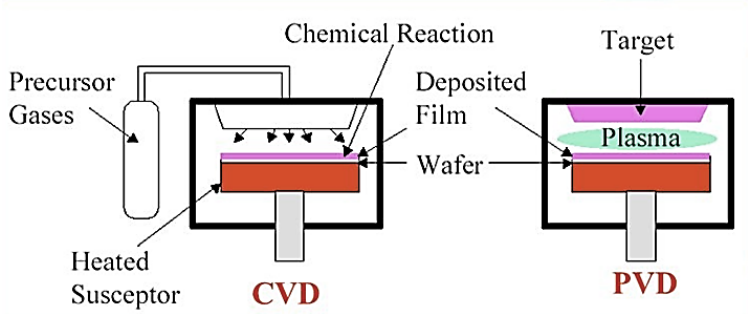

Figure 4.2. General difference between CVD and PVD – adapted from [48].

One of the most basic differences between the procedures is the need to use precursor gases in CVD. For TMDs deposition, the CVD process requires sufficiently volatile precursors, which means that dangerous chemical agents, capable of aggravating the ecological issues, may be produced. Whilst is true that the PVD process requires skilled operators and high monetary capital,

the advantages of PVD outweigh the drawbacks in ambit of this research. Thus, PVD is the general technique debated in this chapter [49].

4.2.1. PVD

PVD represents all deposition processes in which a material (i.e. molecules or atoms) is atomized from a target, in sequence to the latter being hit with energetic ions. These energetic ions can be formed either: i) in a confined plasma or vacuum, for the sputtering process; ii) through high energy electron beams or thermally heated filament, for the evaporation process. In any case, the atomized material travels through vacuum, low pressure gas or plasma, until the substrate, where it condenses [46].

4.2.1.1. Sputtering

Sputtering is a PVD technique, so it follows the steps described in the previous paragraph. First, as charged particles (most often Ar^+ ions) hit the target, sputtering happens, which means there is a removal of atoms from the target. Then, the ejected particles travel towards the substrate. Lastly, the condensation of these particles on the substrate occurs, allowing the film to grow. **Figure 4.3** represents the sputtering process in a simplified manner, process which generally ensures a great quality of the coatings [26, 46, 50].

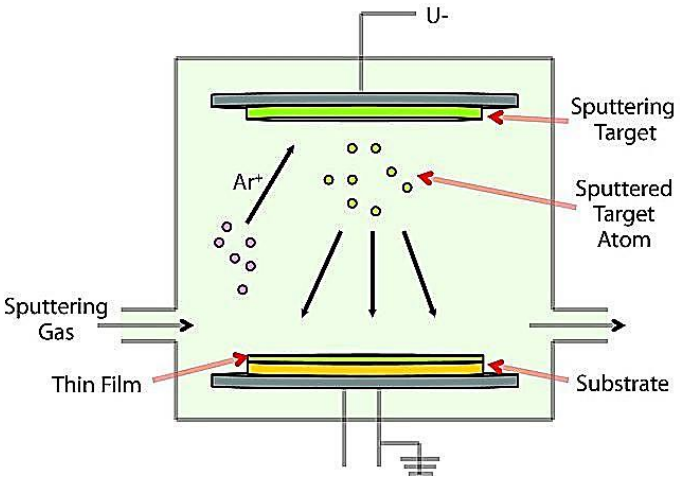

Figure 4.3. Scheme of PVD sputtering process with incident energetic Ar^+ (Argon) ions hitting the target, the atoms removed from it traveling through plasma and depositing on the substrate – adapted from [51].

Not all the particles inside the deposition chamber are atoms sputtered from the target. More rigorously, they are neutral atoms, positive Ar ions, and electrons, as explained in **Figure 4.4**, and contaminants such as residual oxygen. Nonetheless, contaminants are not many inside the deposition chamber, as the common environment for the process is high vacuum and an Ar plasma [26].

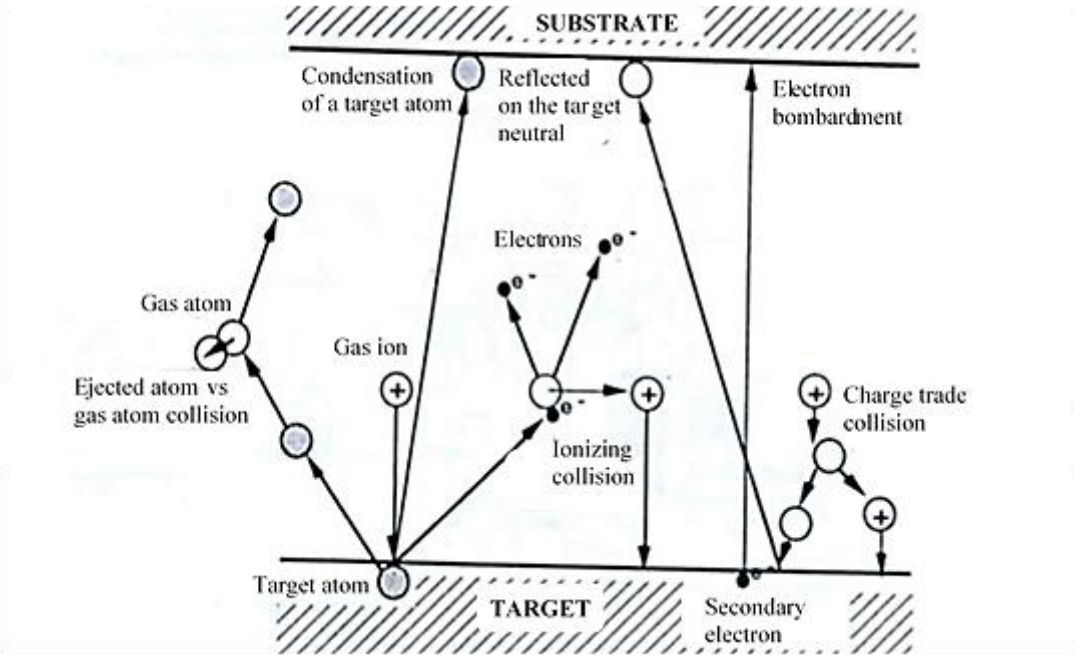

Figure 4.4. All types of particles present in the sputtering technique – adapted from [26].

The Ar plasma inside the deposition chamber is sustained, between the target and the substrate, either by DC (direct current) or RF (radio frequency) alternating current. Generally, RF power mode is utilized to deposit the electrically insulating materials and DC power mode is used to sputter the electrically conductive materials [5, 46]. Sputtering in RF mode improves the deposition stability but the elevated plasma density close to the substrate, shown in that power mode, manifests in an increased bombardment of Ar^+ ions to the substrate, which produces some re-sputtering of the deposited coating. Thus, this mode provides lower deposition rates. Also, because Se is lighter than Mo, it is sputtered preferentially, and the growing coating becomes short in the Se/Mo ratio. [5]. DC mode, on the other hand, provides higher Se/Mo ratio, is more economical and ensures enhanced deposition rates [46]. For all these reasons, DC power is the utilized mode in this work.

4.2.1.1.1. DC Unbalanced Magnetron Sputtering

In a simple DC sputtering system, two electrodes, an anode and a cathode, coexist within a gas filled vacuum chamber. The cathode is covered by target material to be deposited, whilst the anode is where the substrates are placed. When these electrodes are submitted to a voltage difference, and under the right conditions of pressure, a glow discharge appears in the chamber. Then, the Ar^+ gas ions formed in the glow discharge are accelerated in the direction of the target and sputter the target surface. This results in the ejection of target atoms and further deposition of the target material on the substrate, under the form of thin films. In the simple sputtering system, however, the electrons ejected from the cathode are not efficiently used for sustaining the discharge [6, 49]. That is why, for magnetron sputtering system, represented in **Figure 4.5**, by the suitable application of a magnetic field, via an appropriate arrangement of magnets placed behind the target, electrons can be deflected to circulate on a closed path near the surface of this electrode. The consequent high flux of electrons creates a high-density plasma from which ions can be extracted to sputter the target material [46].

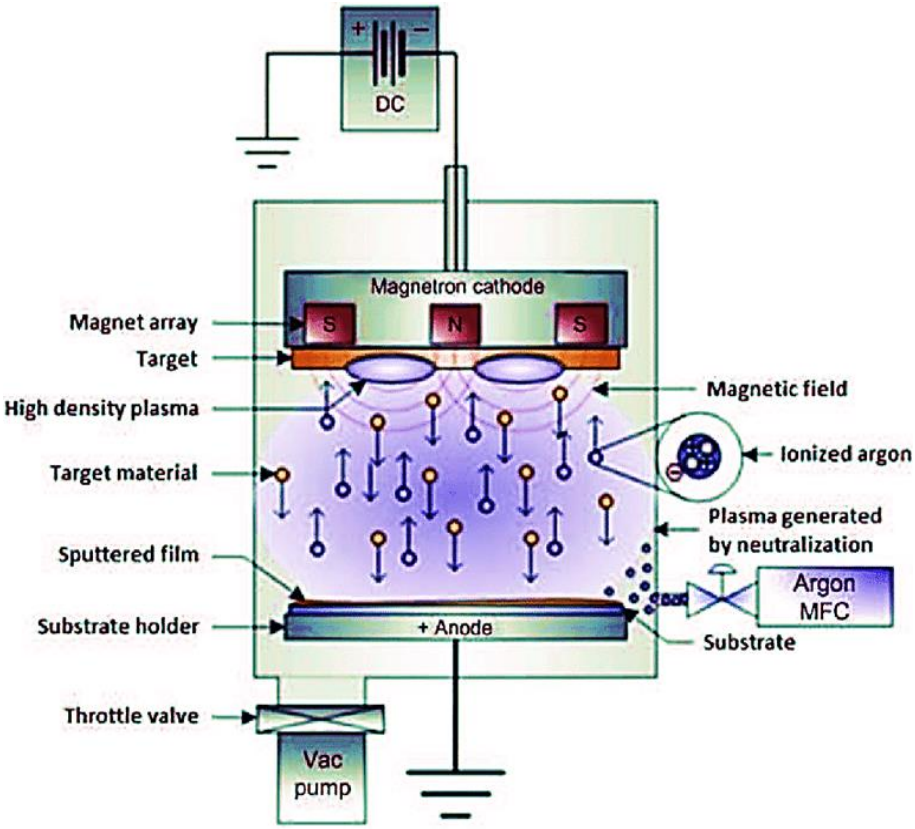

Figure 4.5. DC magnetron sputtering system representation – adapted from [52].

In magnetron sputtering processes, frequently, three rows of permanent magnets are arranged in N-S-N or S-N-S order, with the inner magnet having an opposite polarization than the outer magnets. Additionally, if the inner magnet has a weaker strength, it leads to an “unbalanced” magnetron sputtering system, providing a magnetic field with increased length, that causes higher ionization in Ar plasma and an escape of the electrons from the cathode region, leading to increased ionization of the Ar atoms in the proximity of the substrates. This causes higher resputtering and due to it a requirement for slower deposition rates so that the Se/Mo ratio does not decrease. However, with an unhurried deposition the film compactness is improved. Without paramount interference from the substrate, the correct selection of the deposition parameters originates a coating with a certain thickness. For thicknesses lower than 5 μm, the magnetron sputtering technique guarantees uniform, high-purity films, together with easy industrial scalability. It also permits the achievement of coatings with controlled chemical composition, roughness and density. Surely, the targets can be expensive, and the system is not utterly energy efficient, but advantages of magnetron sputtering clearly compensate its drawbacks in the ambit of this research [53].

In order to conduct this investigation, an unbalanced magnetron sputtering device is utilized, in direct current mode, to deposit the MoSeC films onto M2 steel substrates.

5. EXPERIMENTAL PROCEDURE

The experimental method utilized for pre-deposition and deposition is explained in sequence.

5.1. Pre-Deposition Method

Throughout pre-deposition, samples of high-speed steel AISI (American and Iron Steel Institute) M2, of approximately 9 GPa of hardness, with a diameter of 24 mm and thickness of 8 mm, were prepared for further polishing. Also, Si wafers were cut to be used as substrates for posterior GIXRD analysis.

In sequence, a polishing process of the steel substrates was conducted, via utilization of SiC papers from P120 down to P1200 grit sizes. For improved finishing quality, magnetic backed cloths (6 µm and 3 µm grit sizes) were utilized together with diamond suspensions, adequate for these grit sizes, which filled the polishing cloth. The achieved surface roughness was of R_a < 20 nm. Subsequently, prior to deposition, a process of cleaning ultrasonically in acetone and ethanol, the Si wafers and M2 steel substrates, was carried out. Ultrasonic cleaning lasted about 10 min and then the substrates were ready to be put in the rotating carriers, positioned in the center of the deposition chamber.

5.2. Deposition Method

5.2.1. Equipment and Target-Substrate Distance

To deposit the coatings, a closed-field unbalanced magnetron sputtering equipment, small industrial-scale, with a volume of 275 dm^3, named Teer UDP 650/4, was used.

Four planar targets (380 x 175 x 8 mm), vertically aligned on the chamber walls with a 90° angle between them, were employed, as the scheme of **Figure 5.1** illustrates. Planar targets have advantages and limitations, but they were chosen due to existence in a huge range of tested designs, in varied target materials, at low production costs.

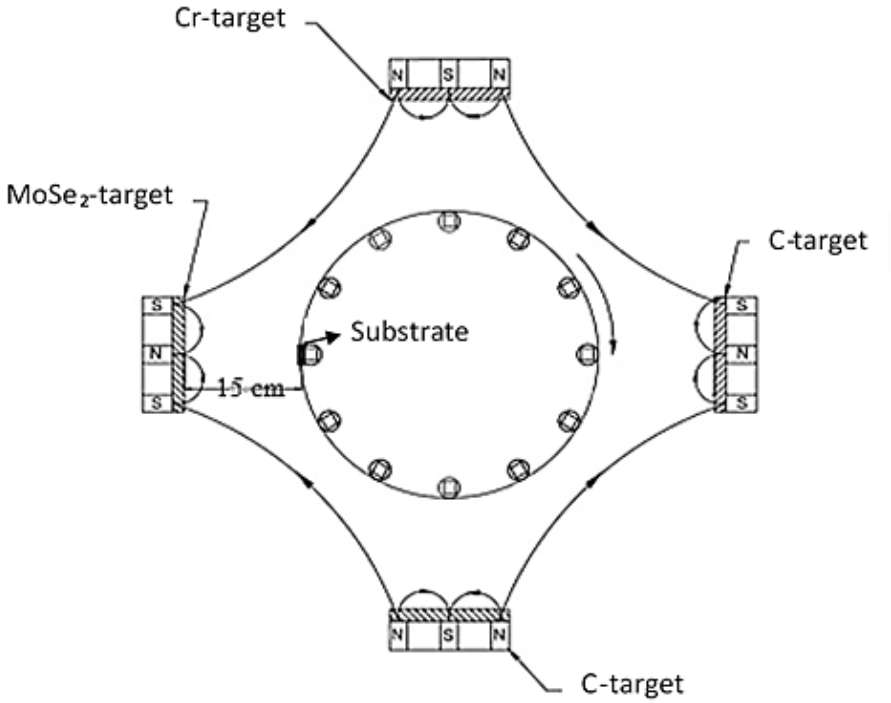

Figure 5.1. Magnetron sputtering system utilized to deposit the MoSeC coatings – - adapted from [1].

The targets used were 1 Cr target, 1 $MoSe_2$ and 2 graphite targets, all with 99.9% purity, whilst the target-substrate distance was 15 cm. The utilization of 2 graphite targets is explained as carbon presents a lower sputtering rate than the other target materials. The target-substrate distance chosen, 15 cm, is a moderate distance, which affords superior tribological performance at high temperatures, as demonstrated in a study performed by Vuchkov et al. [1].

5.2.2. Deposition Process

In a first step, covering shields were applied to each target to prevent cross-contamination from the targets to the substrates during the process. Then, targets and substrates were sputter cleaned. The deposition parameters utilized to clean the targets and substrates are summarized in **Table 5.1**.

Table 5.1. Cleaning parameters applied on targets and substrates, in the deposition process.

	Current Applied (A)	Pulsed Bias Voltage (V)	Frequency (kHz)	Reverse Time (µs)	Cleaning Time (min)
Carbon Targets	1.9	-	-	-	20
$MoSe_2$ Target	1.5	-	-	-	20
Cr Target	4.5	-	-	-	20
Substrates	-	600	250	1.6	40

Pulsed bias voltage, which provides a more confined plasma near its application area, was only applied on the substrates. Thus, the substrates are efficiently cleaned through Ar^+ ion bombardment. The targets are cleaning for 20 minutes each in pairs (e.g. $MoSe_2$ and the opposite graphite, and Cr and its opposite graphite target). The total cleaning time for the substrates is 40 minutes.

After the elucidated cleaning stage, the actual deposition process occurred. For the deposition process a current control mode was employed, which means, targets had a fixed total current applied.

The total deposition time was 120 min. From these, the earliest 10 min were dedicated to the deposition of a Cr interlayer, with 5 A of current applied on the Cr target. The interlayer is expected to provide improved adhesion of the top MoSeC film to the substrate.

Throughout the next 10 min, a gradient layer was deposited, in which the currents applied for both carbon and $MoSe_2$ targets were increased, while for the Cr target the current was decreased. The concept behind this is to foment a gradual transition of the cross-sectional properties between the Cr interlayer and the MoSeC coating.

To complete the total 120 min of the deposition process, 100 min of the MoSeC coating deposition occurred, in which 1 from the 5 distinct carbon contents (6 at. % of C, 24 at. % of C, 33 at. % of C, 51 at. % of C, 60 at. % of C) studied for the purpose of this work, was deposited. The 6 at. % of C coating is also referred as the pure $MoSe_2$ coating, as it is difficult to obtain lessened contents of carbon. The carbon contents of the yielded coatings in the five deposition procedures are ranked almost proportionally to the total current applied on the correspondent targets, as presented in **Table 5.2**.

Table 5.2. The different coatings deposited, and the parameters applied on the deposition stage.

	Current on $MoSe_2$ (A)	Total Current on Carbon Targets (A)	Bias Voltages (V)	Resulting Substrate Current (A)
Pure $MoSe_2$	1.7	-	50	0.06
MoSeC24C	1.7	1.3	50	0.16
MoSeC33C	1.7	2	50	0.23
MoSeC51C	1.7	4.2	50	0.42
MoSeC60C	1.7	6.5	50	0.53

In the course of the 120 min of deposition, the pressure on the chamber was stabilized at 0.4 Pa and the argon flux at 35 sccm (standard cubic centimeters per minute).

After each deposition, every target got switched off, and a process of cooling the chamber was promoted.

On the end of the cooling stage, substrates were removed from the chamber.

5.3. Characterization Techniques

In this thesis, the chemical composition of the deposited coatings was determined via WDS using an Oxford Instruments detector attached to an SEM (Zeiss Merlin).

The thickness and morphology of the films was analyzed with a SEM, in the same equipment.

The crystal structure analysis was performed via an PANalytical X'pert MRD equipment. XRD (X-ray diffraction) was operated in grazing incidence mode, utilizing copper Kα radiation (U = 40 kV, I = 45 mA), at an incident angle of 3°. The scan was performed in a 2θ range of 5°-90°, during 2 h 40 min.

The adhesion of the coatings was evaluated by a scratch test in a CSEM Revetest apparatus, using a conical diamond stylus with a tip radius of 0.2 mm. The stylus was drawn across the sample at a constant velocity of 10 mm/min, and the selected load range varied from 2 to 80 N. The utilized optical microscope for *post facto* inspection of the failure modes was a Leica DM4000 LED.

A Rockwell C indentation test was also conducted, at a Karl Frank GMBH apparatus, with a load of 1471 N applied to the surface of the coating via utilization of a diamond cone Rockwell

C type indenter. The originated crater was then inspected by optical microscopy, to assess the level of adhesion of the coatings, with assistance of the VDI guideline 3198.

NanoTech (Micro-Materials Ltd.) nanoindentation equipment, equipped with a Berkovich diamond pyramid indenter was used to check mechanical properties such as the hardness and reduced elastic modulus of the coatings. Nanoindentations were performed on the free surface of each sample, at shallower depths than 1/10 of the coating thickness, at ambient temperature, with a maximum applied load set at 3 mN.

An AFM Bruker Innova system allowed to represent the surface morphology of the coating (3 nm by 3 nm and 5 nm by 5 nm areas). Aided by the software *Gwyddion* [54], it also enabled to picture the topography and evaluate the roughness of the coatings.

The previously mentioned were non-tribological characterization techniques.

As for tribological characterization techniques, the university-customized POD (pin-on-disk) machine performed experiments in 20 different conditions, all with a fixed sliding velocity of 0.05 m/s, load of 10 N and relative humidity kept in the 40 % +- 5 % range. Given the 5 diverse carbon contents of the coatings, the tests also differed in temperature, 25°C or 200°C, and in the material sliding against the film, which translated into NBR or DIN 100Cr6 steel balls, the latter with a hardness of ~ 7 GPa. At least 2 tests were performed in each of the 20 probed conditions.

Finally, an Alicona Infinite Focus 3D optical profilometer made it possible to calculate the specific wear rate and sliding track width, both related to the wear performance of the coating, on each test condition. This device permitted to measure the sectional area removed from the wear track of the several POD experimented coatings, calculation made by taking the average cross-sectional area removed from 4 profiles, each in one varied region of the worn track. This value was multiplied by the wear track circumference to achieve the worn volume across all the film and was then divided by the sliding distance and the normal applied force [6]. The formulation described above translates into:

$$k = \frac{V}{DF} \tag{5.1}$$

Where V is the worn volume in mm³, D is the sliding distance in m, F is the perpendicular applied force in N and k is the specific wear rate coefficient in mm³/Nm.

All the mentioned characterization techniques in this chapter are further explained in **ANNEX A: BRIEF FUNDAMENTAL THEORY OF THE CHARACTERIZATION TECHNIQUES**, in a short text about each.

6. RESULTS AND DISCUSSION

6.1. Compositional (Chemical), Morphological and Topographical Characterization

6.1.1. Chemical Composition

The chemical composition of the several coatings deposited was obtained via WDS and the results are summarized in **Figure 6.1**.

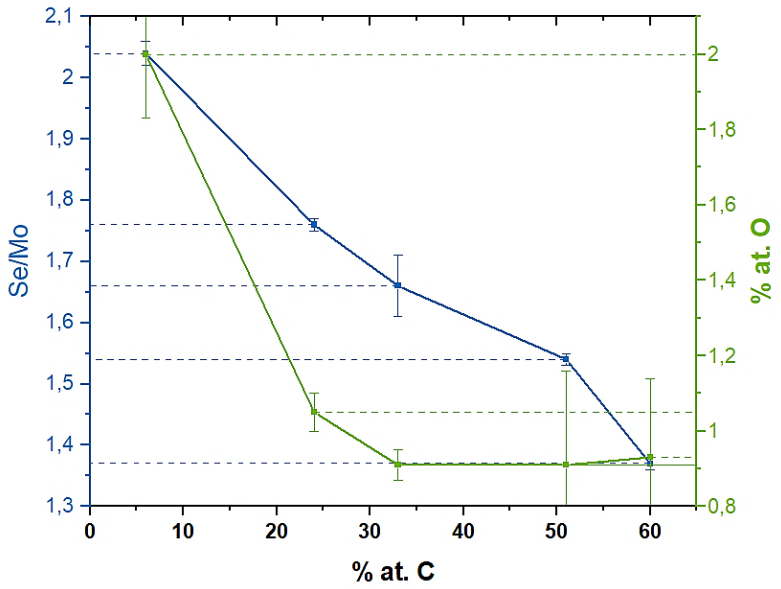

Figure 6.1. Se/Mo ratio and oxygen content for the varied carbon content samples.

As demonstrated, the increase in carbon content in the MoSeC samples deposited generates an almost linear decrease in the Se/Mo ratio, also named stoichiometry of the coatings. This event should manifest in a worse sliding scenario because it can impair the crystallinity of the $MoSe_2$ and thereby its lubricity. If there is low Se content, then the TMD layers might not be so ordered, and Mo-C or MoO_3 phases be more prone to be formed. The reduced Se/Mo ratio for the coatings with high carbon content can further be correlated with a different level of bombardment

of the growing film with energetic species. It is very likely that the high current applied to the graphite targets results in a significantly increased Ar ionization in the proximity of the substrate. Also, with the application of substrate bias the coatings are subjected to higher bombardment, resulting in accelerated preferential resputtering of the lighter Se atoms.

On a dissimilar trend to the Se/Mo ratio, the oxygen content seems to decrease only up to 33 % at. C. For samples with superior carbon contents, despite the enlarged error range, the oxygen presence seems to stabilize, which could be the cause for an approximate plateau in the porosity and respective compactness of the coatings.

6.1.2. Morphology and Topography

The surface morphology and the coatings cross-section and thickness were evaluated by SEM. The images of the surface morphology and cross-section of the coatings are depicted in **Figure 6.2**.

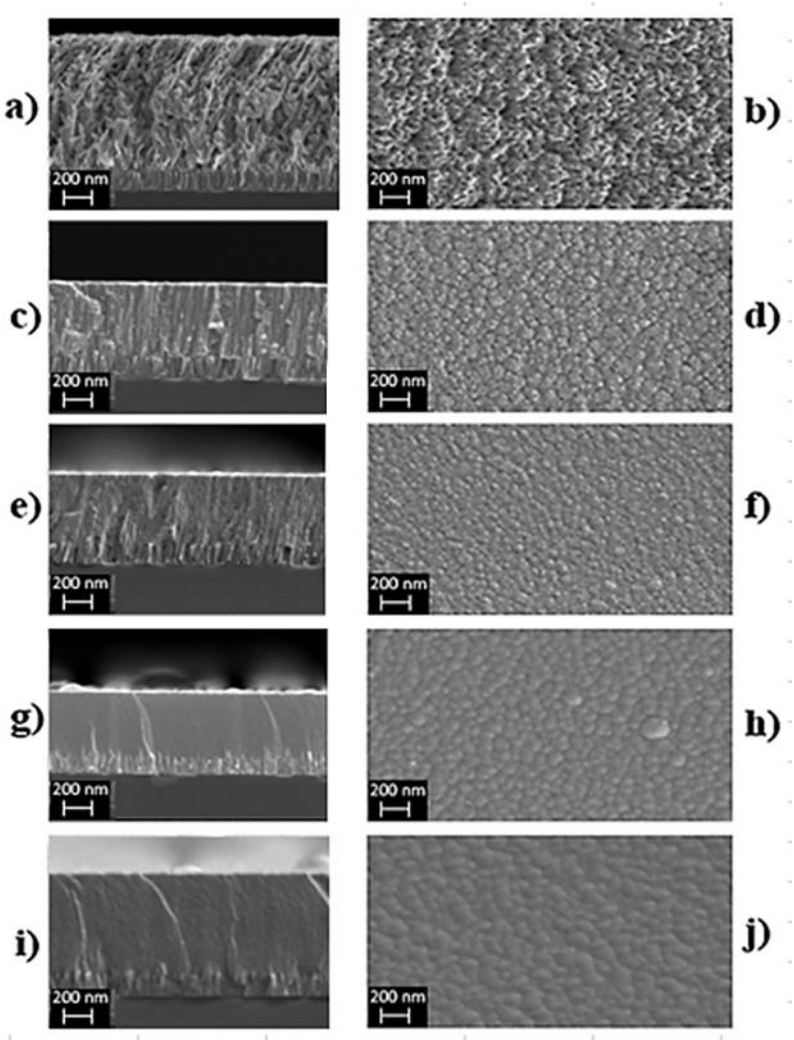

Figure 6.2. Cross section (CS) and surface morphology (SM) of the MoSeC coatings obtained via SEM: a) CS of pure $MoSe_2$; b) SM of pure $MoSe_2$; c) CS of 24 at. % of C; d) SM of 24 at. % of C; e) CS of 33 at. % of C; f) SM of 33 at. % of C; g) CS of 51 at. % of C; h) SM of 51 at. % of C; i) CS of 60 at. % of C; j) SM of 60 at. % of C.

Additionally, topographical images were evaluated by AFM. The topographical images, as approximated by the software *Gwyddion*, are displayed in **Figure 6.3**.

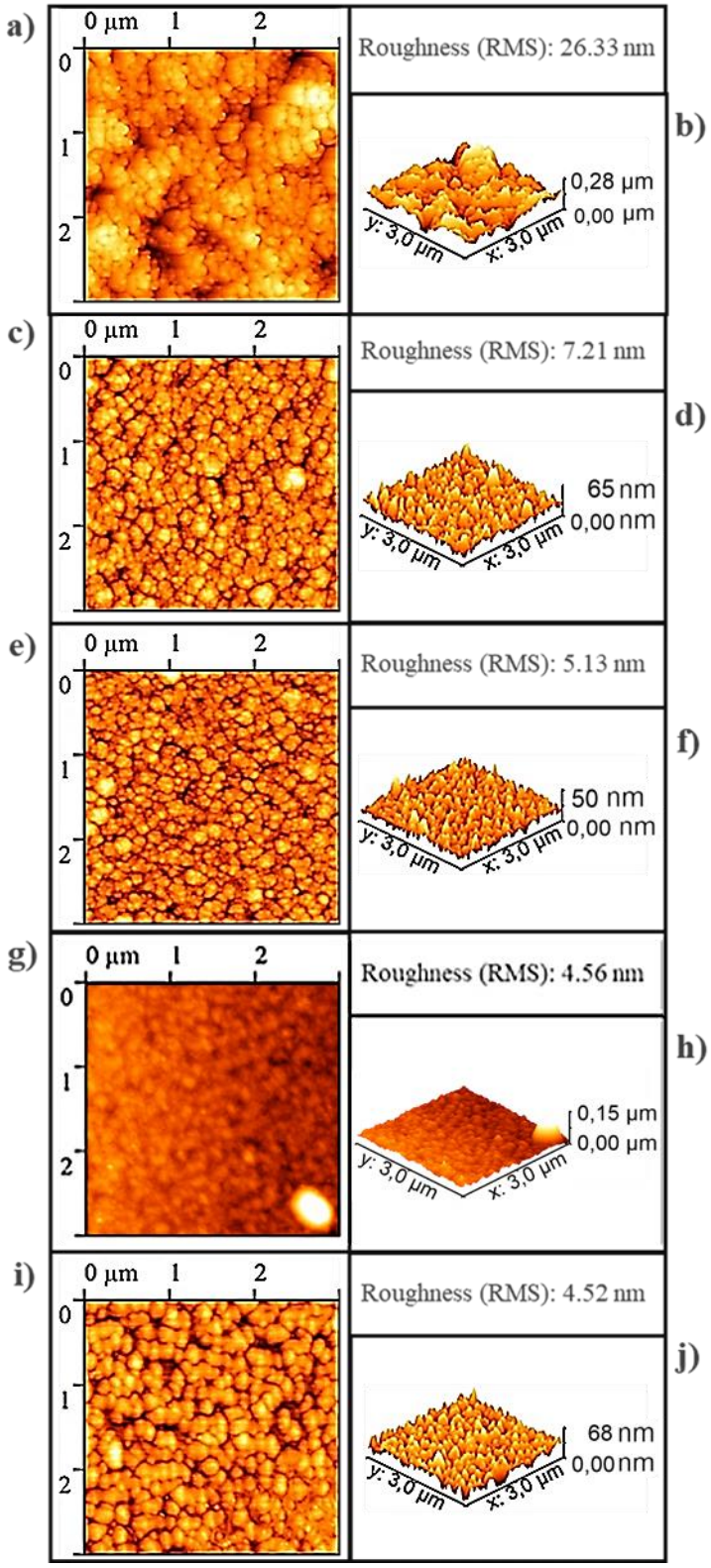

Figure 6.3. AFM surface morphology (ASM) and 3D topography (T) of the several coatings deposited: a) ASM of pure $MoSe_2$; b) T of pure $MoSe_2$; c) ASM of 24 at. % of C; d) T of 24 at. % of C; e) ASM of 33 at. % of C; f) T of 33 at. % of C; g) ASM of 51 at. % of C; h) T of 51 at. % of C; i) ASM of 60 at. % of C; j) T of 60 at. % of C.

Both SEM and AFM confirm that the pure $MoSe_2$ displays a cross section with columnar structures and a relevant porosity between the columns. The elevated average roughness and darker surface areas shown in AFM confirm the shadowing effects related to the columnar structure, depiction also perceptible in SEM cross-sectional pictures. These structures are usual in pure sputtered TMDs. Moreover, the pure coatings show a sponge like surface morphology, highly porous, as seen in SEM surface morphology images and in previous works of Yaqub et. al. [3, 5].

With carbon introduction in the coatings, the columnar cross-sectional structure is maintained, although the coatings start to present a much more compact morphology, with less voids between columns, and a more homogeneous structure. This is valid until the 60 at. % of C, as confirmed by both SEM and AFM surface morphology images. The mentioned surface morphology transformation also manifests in a granular cauliflower-like appearance for the coatings with some carbon presence, like the 24 at. % of C and 33 at. % of C films, whilst in an akin to dome-grain morphology for the 51 % and 60 at. % of C coatings.

An explanation for the shift from sponge-like surface features, in the pure $MoSe_2$ coatings, to compact morphologies, such as the cauliflower type morphology or an akin to dome-grain morphology, in the coatings with certain carbon presence, is believed to be generated by an increased surface mobility that influences the growth of the coatings. The higher current applied to the carbon targets may manifest in an elevated temperature at the surface of the films and, as previously discussed, a higher bombardment of the growing film with Ar^+ ions, which induces higher adatoms (atoms deposited on the substrates, that are right above the film surface) mobility and, consequently, increases the atomic coverage of the coatings surface, enhancing the density of the films [1].

Further, the thickness of the coatings is checked in **Table 6.1**.

Table 6.1. Thickness of the coatings based on cross-sectional SEM measurements.

	Thickness (µm)	**Deposition Rate (nm/min)**
Pure $MoSe_2$	2.7	22.5
MoSeC24C	1.2	10
MoSeC33C	1.1	9
MoSeC51C	1.3	11
MoSeC60C	1.6	13.5

The thickness of the coatings lowered until the 33 at. % of C film and increased for the two coatings ameliorated in carbon. The latter statement is probably occurring due to the existence of a similar compactness in higher carbon content coatings (over 33 at. % of C) while way higher rates of deposition in the 51 at. % of C and 60 at. % of C films.

To sum up, based on the results obtained in SEM and AFM techniques, the optimal range for carbon should lay between the 33 at. % of C coating and the 60 at. % of C, as these coatings present a relatively close density and surface compactness, as shown by the surface morphology in AFM or SEM. Moreover, the ideal content must be closer to 51 or 60 at. % of C due to the slightly discrepant SEM cross section illustration when compared to the 33 at. % of C film. A neat, unbeneficial, columnar structure only appears up to the 33 at. % of C coating.

6.2. Structural Characterization

6.2.1. Crystal Structure

The crystallography of the coating was studied via GIXRD. The results are presented in **Figure 6.4**.

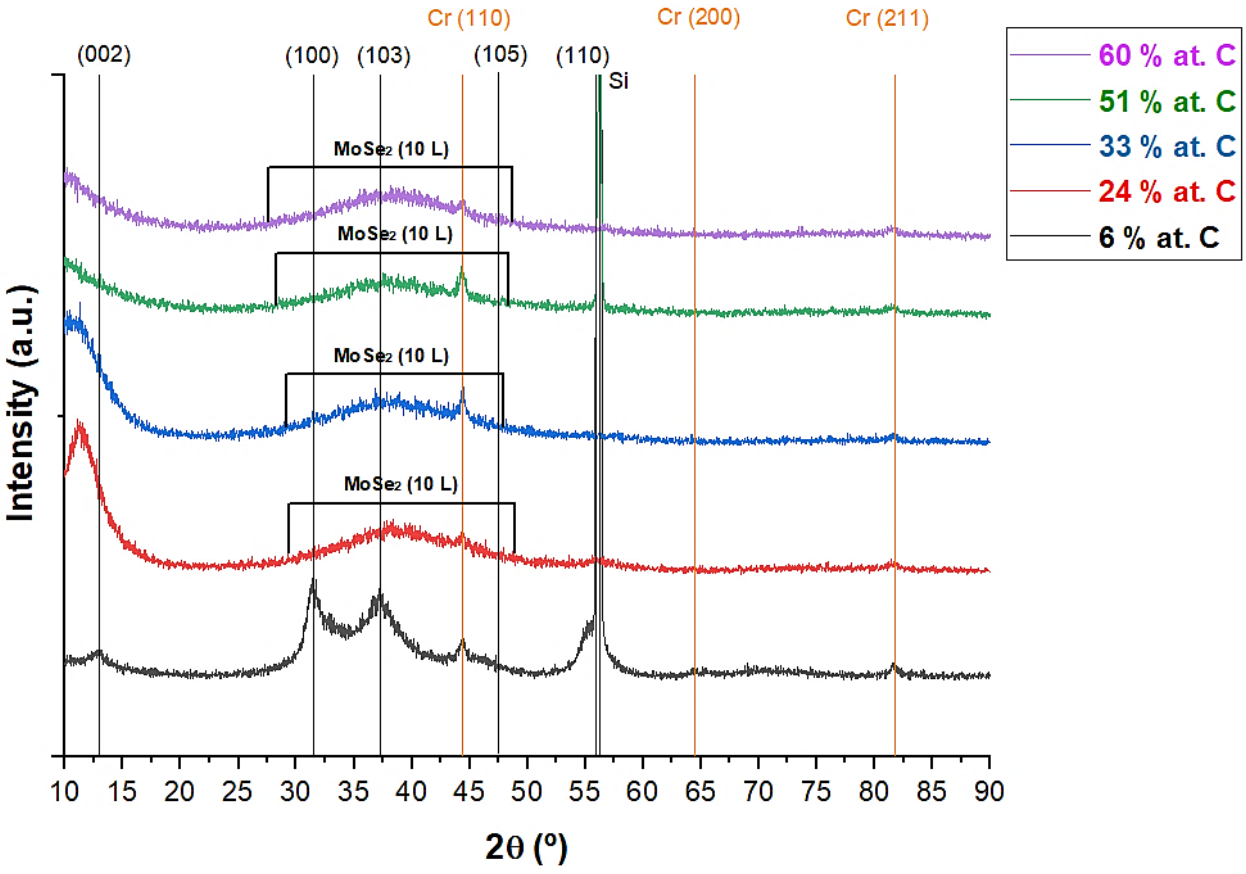

Figure 6.4. Results from the GIXRD diffractogram for all the samples.

The GIXRD diffractogram presents several $MoSe_2$ orientations with the strongest diffractions occurring for basal planes orientation of (002) at 2θ ~ 13°, of (100) at 2θ ~ 31.5°, of (103) at 2θ ~ 37.5°, of (105) at 2θ ~ 47.5º and of (110) at 2θ ~ 56° (Reference ICCD card No. 01-0771715). Additional peaks stemming from the Cr interlayers were observed at 2θ ~ 44.5°, 2θ ~ 64.5° and 2θ ~ 82° (Reference ICCD card No. 01-0851335). Phases with fairly low grain size are very small to be detected through GIXRD analysis, which means that nanograins, such as Mo-C particles, could not be identified [3].

To determine the GIXRD peaks, the reliable Scherrer formula was utilized. From this method, when a peak is broader, the crystallites are smaller, meaning the coating is tendentially more compact and amorphous [32]. GIXRD patterns displayed a loss of crystallinity in MoSeC when carbon content in the coatings was increased. In this study, this concept is further represented for the carbon coatings, approximately between 30° and 50°, by the turbostratic stacking of the $MoSe_2$ (10 L) planes, with L taking the values of 1, 2, 3, 4, etc, which signifies that the usual ABAB hexagonal stacking may suffer translations or rotations relative to its most ordered structure [27, 55].

An enhancement of the carbon content in the samples also translated in a shift of the (002) peaks position to lower angles, due to a rise in the TMD interplanar distance, event which roots diminished van der Waals adhesive forces between TMD basal planes and can facilitate the easy shearing properties of $MoSe_2$ [5]. Despite the increase in interplanar distance, the thickness of the coatings from the pure coating to the 33 at. % of C film decreased, suggesting more compact coatings for higher carbon contents, result which agrees with reported literature. A probable explanation for this is that for higher carbon content coatings, there are smaller $MoSe_2$ crystallites, as suggested by the broader (002) peaks in the higher carbon content samples. Hypothetically, carbon must disturb the growth of the $MoSe_2$ crystals [3], thus inducing the thickness of the coatings to decrease, although the interplanar distances follow the inverse path, possibly due to an entrapment of the carbon within the interplanar space.

Both compactness and (002) orientation of basal planes are positively correlated with improved friction behaviour. So, the 33 % at. C coating seems to highlight in the GIXRD analysis, as compared to the other coatings. Not only it has good compactness, but also its (002) orientation is well pronounced. Despite, the (002) orientation has much lower surface energies than the (100) orientation, thus, atoms deposited on the (002) oriented surface have superior odds of being re-sputtered before adsorption of following incident target material [56]. So, the higher the (002) orientation, the more importance the rate of film deposition assumes.

Also, even though the (002) orientation has higher tendency for shifting with the variation in the at. % of C, and thus the presented conclusions caused by the (002) peaks position tendential shift are probably valid, it must be noted, as a purely mathematical statement, that the exact positions of the mentioned peaks might not be fully accurate as, when θ decreases, an error in this angle determination causes an increased error in the sin(θ) introduced in the Bragg's equation (represented in **Figure A.3**), which may provoke slightly wrong cell parameter (like the d, which means interplanar distance) calculations.

6.3. Mechanical Characterization

6.3.1. Hardness

Both hardness and reduced Young's modulus are two fundamental mechanical properties which can be obtained, with precision, via Nanoindentation.

Therefore, the average results for both hardness and reduced Young's modulus, for the varied carbon content samples, are represented in **Figure 6.5**.

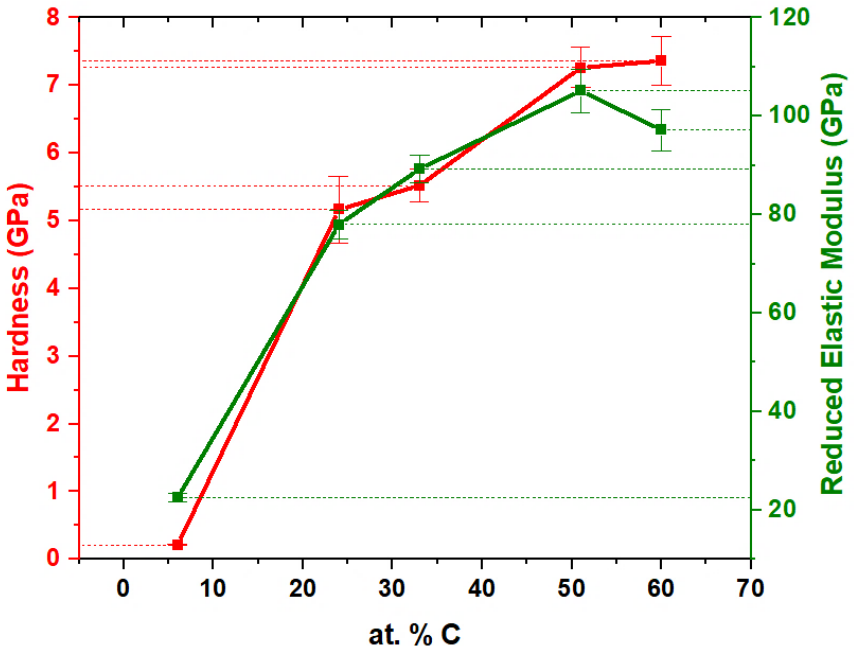

Figure 6.5. Results from the Nanoindentation test: hardness and reduced elastic modulus, for each carbon content.

The results are quite similar for both properties. The values increase for superior carbon contents, although a slight nuance occurs for the elastic modulus, in the superior carbon contents.

Owing to a low density and high porosity, the pure $MoSe_2$ coating displays a very low hardness of about 0.25 GPa, and an equally low reduced Young's modulus of about 21 GPa. Claims of the literature, that a higher Se/Mo ratio contributes to a lower hardness, are also verified, as in the pure coating, this ratio is the highest, with about 2.04 [1].

Increasing the carbon content in the coatings, the compactness of MoSeC coatings is enhanced as well, and the hardness and reduced Young's modulus values reflect that. In fact, for the 24 at. % of C film, the hardness goes up to ~5 GPa, almost twenty-fold the values observed for the pure coating, and the modulus also increases considerably from 21 GPa to 79.5 GPa. Thus, a low carbon addition immediately enhances the coating mechanical performance by a large amount, result which agrees with literature reports referring that embedding the soft $MoSe_2$ in a carbon

matrix contributes to increases in both parameters [4]. For the 33 at. % of C coating, the values of both properties are in the error range of the immediately lower carbon content film.

Then, the 51 at. % of C coating presents the highest reduced Young's modulus value, of 105 GPa, which decreases to 98 GPa in the 60 at. % of C film. Although the hardness stayed in the error margins for the 60 at. % of C coating as compared to the previous 51 at. % of C coating and the reduced Young's modulus followed the same trend, the latter property did not manifest exactly the same variation as the former. Concretely, the elastic modulus lowered reasonably for the highest carbon content. This phenomenon may be explained by the low Se/Mo ratio, which decreased significantly from 1.54 to 1.37 between the 51 % at. C and the 60 % at. C films, respectively, thus increasing the hardness but not the elastic modulus. Additionally, the compactness of the coatings may come to an approximate plateau between the range of 33 at. % of C and 60 at. % of C. The latter thought is induced by the non-increase in the modulus that should otherwise follow the hardness tendency for the superior carbon content coatings, since higher compactness usually translates into improved Young's modulus because the last property measures a pressure divided by a strain [57]. With a constant pressure, the strain produced on a more compact coating should generally be lower. Also, the presented hypothesis for the compactness plateau agrees with the fact that all three higher carbon content coatings display similar oxygen contents. The SEM images, manifested in similar morphological features amongst the mentioned coatings, concur too with the mentioned assumption. Summing up, if the three increased carbon content films have similar compactness then it is predictable that the modulus does not follow the hardness proportionality with the at. % of C. Despite the seemingly poorer results in the 60 % at. C coating, it may be a favorable occurrence that the hardness does not change much, and the reduced modulus is lower, as the H^3/E^{*2} ratio, with E* being the reduced Young's modulus, is higher for 60 at. % of C than for 51 at. % of C, which indicates the existence of a higher fracture toughness of the coating, avoiding crack propagation, and the possibility for a higher adhesion strength as well [5].

6.3.2. Adhesion

As discussed in **3.2.2.3**, the Cr interlayer, between the coating-substrate pair, is necessary for the coating to display enhanced adhesion and not peel-off from the substrate.

The adhesion strength was assessed by two methods: i) Scratch test and ii) Rockwell C Indentation.

Even though the Lc (critical load) depends on several factors, such as the stylus-tip radius, the load rate or the coating thickness, it mostly depends on the coating-substrate adhesion.

The Lc allows the distinction between i) cohesive failures, related to through thickness cracks, as chevron cracks are an example of, from ii) adhesive failures, that are generated by compressive stresses which separate the coating from the substrate, like spallation and buckling are examples of. While cohesive properties refer to failure inside the coating region, adhesive properties are related to the adhesion of the coating-substrate at the interface [58].

Three major types of critical loads exist: chevron cracks or Lc1 failure events, buckling and spallation or Lc2, and gross delamination of the coating on the full scratch width or Lc3 [58].

In this thesis, 3 scratches were performed on each sample surface, in order to test the reproducibility and uniformity of the adhesion strength throughout the whole substrate-coating interfaces. The results are presented in **Table 6.2**.

Table 6.2. Average critical load at which each failure event occurred on the 5 samples deposited, with different carbon contents, in the scratch test.

	Lc1 [N]	**Lc2 [N]**	**Lc3 [N]**
Pure $MoSe_2$	-	-	6.5 ($\pm$ 0.5)
MoSeC24C	-	-	11 ($\pm$ 1.5)
MoSeC33C	-	-	19 ($\pm$ 1)
MoSeC51C	-	26 ($\pm$ 0.5)	> 80 N
MoSeC60C	38 ($\pm$ 1)	43 ($\pm$ 1)	> 80 N

A clear trend is observed. As the carbon content of the coatings increases, the failure event associated with the respective coating only occurs at higher loads and, gradually, moves from adhesive to cohesive failure event. Thus, the coatings with higher carbon content display better adhesion than the ones with lower carbon contents. For the softer coatings: pure $MoSe_2$, 24 at. % of C and 33 at. % of C, the only detected failure event is adhesive Lc3, which promotes gross delamination of the coating from the substrate. Sequentially, in the 51 at. % of C coating, the failure becomes Lc2, and, finally, in the superior carbon content coating, the adhesion strength is undoubtedly the highest of all the samples, as it displays a new onset type of failure, the cohesive one (Lc1).

Pure $MoSe_2$ displays huge delamination of the coating. Due to small hardness, these coatings are even plouwed away from the scratch scar, meaning they are insatisfatory coatings in terms of adhesion strength. Then, the 24 at. % of C and 33 at. % of C coatings show reasonable improvements in adhesion, yet remaining very far from the intended values. Only from the 51 at. % of C film to upper carbon coatings, the films present a considerable improvement in adhesion.

No gross detachment of the coating is detected, only some controlled spalling. However, it is the 60 at. % of C coating that provides an excelled guarantee of acceptance, with spalling occuring at relatively high loads, and even chevron cracks, which begin late in the scar track.

The inset of the failure events, for the varied content coatings, can be distinguished in **Figure 6.6**.

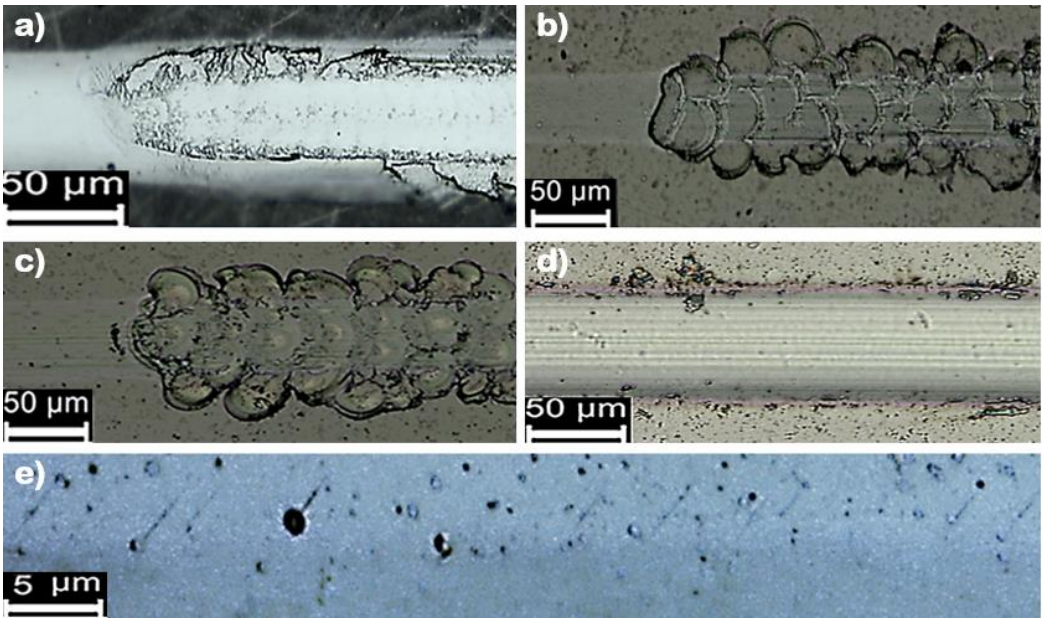

Figure 6.6. Scratch test observations on the optical microscope: a) pure $MoSe_2$ coating, Lc3 inset; b) 24 at. % of C, Lc3 inset; c) 33 at. % of C, Lc3 inset; d) 51 at. % of C, Lc2 inset; e) 60 at. % of C, Lc1 inset.

Similar trends in adhesion as the ones analyzed in the scratch test, are also verified in the Rockwell C Indentation test. The coatings with higher carbon present the best adhesion strength, likely due to the elevated hardness.

Below, the results of the Rockwell C Indentation test are presented, and the subjective scale, from HF1 to HF6, classifying from better to worse adhesion, is attributed to every coating. Scale HF6 is attributed to the pure $MoSe_2$ coating due to complete exposure of the substrate in the immediate region of the indentation. HF5 is the classification given to the 24 at. % of C coating as a visible delamination occurs in the vicinity of the indentation. In a slightly better level of adhesion, the 33 at. % of C film displays large spalled areas, although there is much less visible delamination and exposure of the substrate beneath the coating. The other two coatings, with 51 % at. C and 60 % at. C show a vast improvement in adhesion strength, with only some minor spalling and cracking

around the circumference of the indentation. Both are considered as HF2 level. All this is summarized in **Figure 6.7**.

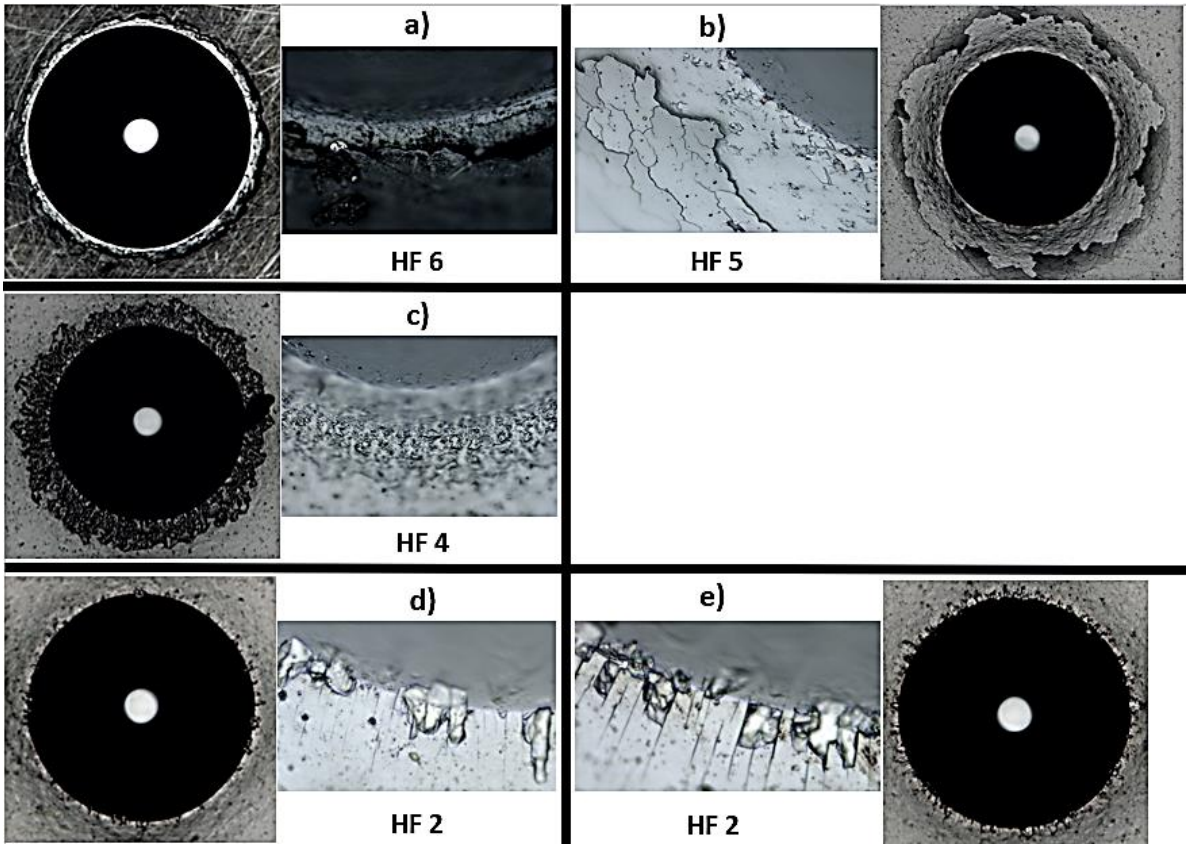

Figure 6.7. Rockwell C Indentations observed at the optical microscope for the correspondent film: a) pure $MoSe_2$; b) 24 at. % of C; c) 33 at. % of C; d) 51 at. % of C; e) 60 at. % of C.

6.4. Tribological Characterization

6.4.1. Friction

In order to characterize the different MoSeC coatings, in terms of their friction behavior when sliding against different materials, POD tests were carried out.

The experiments were performed both versus 100Cr6 steel and NBR countersurfaces and the temperature condition varied between room temperature and elevated temperature. Given that 5 varied carbon coatings were examined, a total number of 20 tests were processed. Additionally, at least 2 repetitions were conducted for each of these 20 dissimilar situations, to

allow for repeatability of the results. All other conditions of a typical POD experiment such as the sliding velocity, load and humidity were sustained in a feasible constant level during the distinct tests, as already mentioned in **5.3**. Particularly, the humidity in the room was important to keep in the smallest range of variation possible, as its increase could be detrimental for the CoF.

In **Figure 6.8**, the outcomes of the POD tests are translated in terms of friction curves (CoF vs sliding cycles).

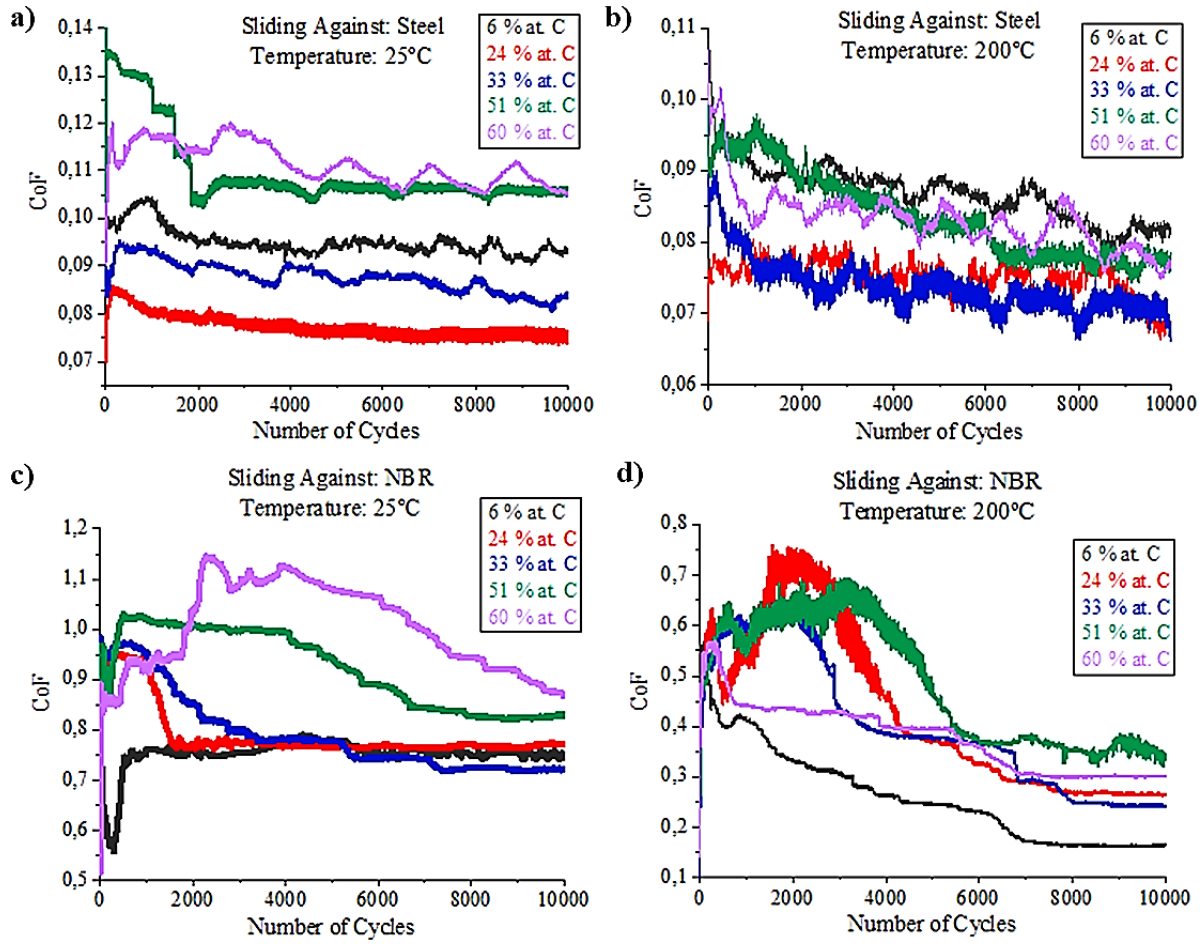

Figure 6.8. POD tests for coatings with all carbon contents (pure $MoSe_2$, 24 %, 33 %, 51 % and 60 at. % of C) performed against steel countersurface: a) at 25°C; b) at 200°C; and conducted against NBR countersurface: c) at 25°C; d) at 200°C.

The friction curves represented above can be divided into 2 main stages: the running-in and the steady-state. In the running-in stage the CoF is typically unstable and displays relatively higher friction values. Subsequentially, the CoF generally follows a continuous drop until the steady-

state period is reached. This second stage is usually characterized by a more constant average CoF, which is then the usually reported value for comparison purposes [59].

Before stepping into a discussion of the friction curve results obtained, the final reached CoF at 10000 cycles is shown below, in **Figure 6.9**, in a neater approach.

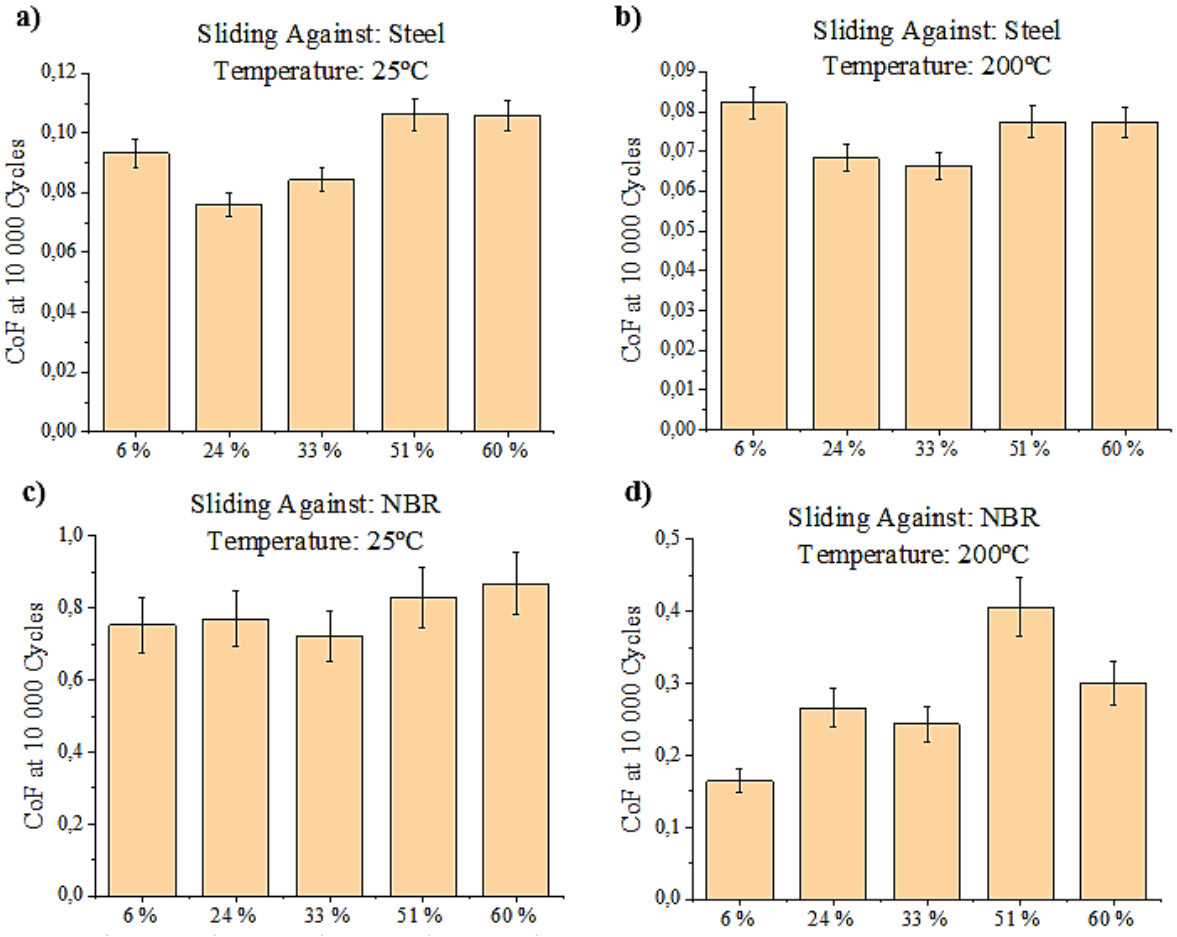

Figure 6.9. Achieved CoF at 10 000 cycles for the 5 carbon contents (pure $MoSe_2$, 24 at. % of C, 33 at. % of C, 51 at. % of C, 60 at. % of C), at 25°C: a) against DIN 100Cr6 Steel; c) against NBR; and at 200°C: b) against DIN 100Cr6 Steel; d) against NBR.

Varied general conclusions can be taken from the combination of **Figure 6.8** and **Figure 6.9**.

In the first place, it is noticeable that when NBR was the countersurface sliding against the MoSeC coatings, the friction was particularly high, and the friction curves revealed instability. This was especially observed in the NBR room temperature tests, in which the final CoF values were on the range of 0.72-0.87, while a span of 0.16-0.41 was achieved for the higher temperature

experiments. The steel tests led to much lower CoF results, of about 0.07-0.10 for room temperature experiments and 0.06-0.08 for high temperature tests. The higher friction results against NBR, as opposed to the steel countersurfaces, are typical since rubber is a much softer material than steel. This property means that rubber surface asperities deform elastically to increase the contact area with the MoSeC film surface. This, consequently, increases friction, due to the accepted Greenwood and Williamson model [60], which amongst other conclusions states that the friction force is proportional to the contact area between the sliding surfaces.

In addition, for both NBR and steel countersurface tests, the conducted experiments revealed an increased of CoF for room temperature conditions relative to the higher temperature tests. Despite the temperature factor was not such a differentiating variable as the sliding countersurface material, since it translated in a lower relative influence on the CoF, the high temperature tests still promoted a lower CoF than the room temperature ones. In the case of NBR countersurface materials, this can be explained by the hysteretic friction component, which is reduced at higher temperatures. In a more general approach, it likely occurred due to a renewed ease for the TMD basal planes to slip which consequentially brought lower friction of the coatings. Why the ease? The elevated thermal energy input at higher temperatures entails the formation, between the coating and ball surfaces, of a thin $MoSe_2$ tribofilm on the contact zone and its self-alignment in a direction parallel to the sliding direction. As a random orientation of the basal planes was detected for the as-sputtered coatings, the alignment mechanism is a reorientation process [4]. It occurs whenever the coating withstands a certain applied load normal to the sliding direction. Once the tribolayer forms, it is the responsible phase for sliding, and brings the possibility to obtain easy shear and a steady low CoF [1, 3].

This thin tribolayer is usually only about 5 nm thick, and is rich in Mo and Se, with carbon being almost absent of the contact zone. Nonetheless, the carbon presence augments with depth beneath the outermost surface of the wear track. So, even though carbon is not available on the top surface of the coating, this phase is fundamental to improve the hardness and load-bearing capacity of the coating, ultimately allowing to provide an ameliorated friction behavior [4]. Moreover, at high temperature, the carbon phase may graphitize in the sliding region, which is another contributive variable to lower the shear strength, as graphite is a good solid lubricant in humid air. The graphitization, however, is not aimed since it lowers the hardness and the load-bearing capacity of the film [34].

For WSC coatings, Raju et al [34] went further to report that high temperature not only decreases the CoF for all carbon contents of the films, as it seems to cause a higher decrease of the

CoF to the higher at. % of C coatings as well. Indeed, in this investigation, all coatings appear to decrease the CoF in approximately the same amount, with exception on the pure $MoSe_2$ coating, which has lower reduction of the CoF than medium carbon content coatings, and on the 60 at. % of C coating, which has an even more increased reduction of CoF, as compared to the other films. So, the outcomes of this study also confirm the hypothesized effect.

Above, the general tendencies of the distinct friction tests were analyzed. However, the actual friction curves still lack debate. To begin the alluded discussion, whether the sliding countersurface was NBR or steel, between the initial running-in stage and the steady-state friction period there occurs a continuous drop of the CoF, which indicates that the tribolayers are being established in relatively thick platelets right beneath the film surface [1]. For NBR this process takes longer than for steel, due to a very diminished hardness of the NBR ball, as compared to the steel ball. Moreover, but in a comparatively smaller contribution to that of the countersurface material, the higher the carbon content of the films and, thus, the harder they are relative to the countersurface material, the longer the steady state seems to take to be reached. Also, on the contrary to the pattern observed for the change of both coating and countersurface material chemical composition, a temperature variation does not seem to have a clear influence on the number of cycles taken to reach the steady state.

On a further scrutiny to the friction curves, no spikes were detected in the CoF graphs for the pure coating. Thus, it is expected that the Cr interlayer and the substrate beneath the MoSeC film were not reached, in the pure $MoSe_2$ film. A spike in the CoF curves means that metal-to-metal contact is present and deteriorates the friction performance of the coatings. This would be plausible to happen in the pure $MoSe_2$ films, since they display very reduced hardness and tend to have way larger wear rates. However, in this investigation, another reason must have caused the slightly increased friction in the pure $MoSe_2$ in comparison with the low carbon content coatings [1].

6.4.2. Wear

To provide a reasonable comparative examination of the wear behavior of the coatings, the friction track descendant from the POD tests was inspected and allowed to quantify the specific wear rate of each film used in a different POD experiment. The aforementioned coefficient provides a fine estimator of the wear rate of each film, as it allows to normalize different test conditions of the tribological experiment, such as the sliding distance, hence the velocity and time, and also the normal applied load, in only a final result.

In **Figure 6.10**, the specific wear rates are appraised, only for the coatings which slid against each of the steel countersurface POD tests. One motif for this is that the NBR ball did not provoke much wear in the coatings, as it has much lower hardness than all the films employed in POD.

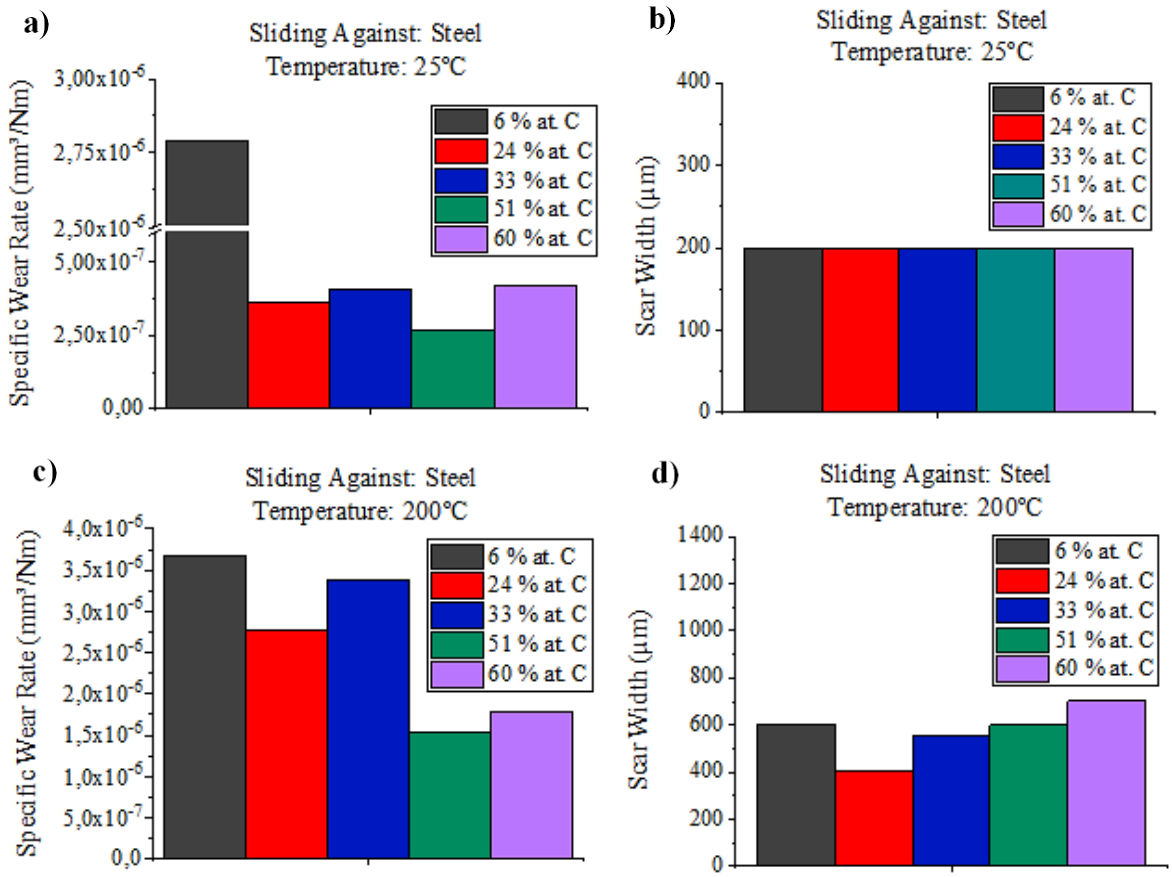

Figure 6.10. Specific wear rates for the films sliding against steel in the POD experiments, i.e. for all carbon contents, against a steel countersurface: a) at 25°C; c) at 200°C; and scar width probed for the same coatings: b) at 25°C; d) at 200°C.

The clearest fact observed in the outcomes displayed above is that both at room temperature and high temperature the lowest absolute wear rates were reached for an intermediate carbon content coating, with around 51 at. % of C, which is coherent with another research [4]. Why that coating? Other than the immediate hardness factor, which explains why the higher at. % of C films should have decreased wear rates, it is noteworthy that this coating was the one with higher elastic modulus, even stiffer than the 60 at. % of C which is a harder coating. Due to being stiffer, the friction area in the 51 at. % of C coating surface shall be decreased, which must

translate into a lower friction force, according to the Greenwood and Williamson Model [60]. Additionally, it was remarked from the SEM techniques that the 51 at. % of C coating seemed to be one of the most compact of all the films. So, the low wear in these coatings might also signify that, even though the particles are plowed, they have more difficulty to move away from their original position and thus are sustained in the sliding track before the end of correspondent test cycles.

Another perceived result is that the wear rate is augmented for higher temperature conditions, although much less for the pure coatings. In other words, the decrease of wear rate from the pure coating to higher carbon content films at 200°C was not as high as the reduction experienced at 25°C. This may also be an indicator that the temperatures achieved for the high temperature experiments afforded an enhanced oxidation of the $MoSe_2$ in the sliding region and led to a graphitization of the carbon phase. Because graphite presents a lower shear strength than the as-sputtered amorphous carbon, the worn particles slide more easily towards the exterior of the friction track and additional wear is fomented [1].

Too, as opposed to what was reported for W-S-C coatings, the MoSeC coatings did not reveal a neat correspondence between the wear and friction results. In fact, the wear rates were lower in the elevated carbon content coatings, contrary to what was visualized in the CoF outcome, which has showed that higher friction occurred in the same films. In this case, a possible reason is the high hardness, which does not worsen the friction problem yet retards the material loss, providing ameliorated wear resistance [3]. However, the worn scar width results at the 200°C POD experiments, show a steep correlation with the CoF. In this instance, the higher the friction the more increased track width was obtained for the same films. The probable scenario was that an increased graphitization influence occurred in these higher carbon content coatings, that led to larger track widths.

7. CONCLUSIONS

MoSeC thin films have potential to be good self-adaptive and solid lubricating materials in applications where low COF is required. Besides the prospective to afford easy demolding in the manufacturing of polymers, it can extend capabilities to the automotive, aerospace or tool industries. Hence, the presented manuscript focuses on the mechanical and tribological characterization of MoSeC coatings with several contents of carbon (ranging from 6 to 60 at. % of C) deposited by DC unbalanced magnetron sputtering. The investigation allows to comprehend how much carbon must be doped in order to deploy a MoSeC thin film capable of the best tribological performance both at 25°C and 200°C, in ambient air, whilst also guaranteeing a fair mechanical behavior, i.e. coatings with elevated stoichiometry, hardness, density and elastic modulus, high adhesion to the substrate and increased degree of amorphization and compactness.

Therefore, in order to characterize the coatings, several techniques were employed. From WDS, a decrease in the Se/Mo ratio with an increasing carbon content of the films was assessed. The % of at. O followed the same trend but was found to decrease only up to the 33 % at. C film. From that carbon content, the oxygen stabilized, which might uncover a similar porosity between the 33 % and 60 at. % of C coatings. The SEM and AFM techniques probed a columnar cross-sectional growth with high porosity and roughness for the pure $MoSe_2$ films but less voids and a continuously more homogeneous and compact morphology for medium and high carbon content coatings. The thickness of the coatings decreased until the 33 at. % of C film and increased for the two coatings with the highest in carbon contents, argument influenced by the similar compactness and higher rates of deposition in the 51 at. % of C and 60 at. % of C films. The GIXRD patterns allowed to remark a higher amorphization for increased carbon content coatings. Crystalline $MoSe_2$ was detected up to a carbon content of 33 at. % and increasing the carbon content resulted in X-ray amorphous structures. From the scratch test, for elevated carbon content coatings, the failure events occurred at higher loads and gradually moved from adhesive to cohesive. Rockwell C Indentation confirmed the scratch test results, with 51 at. % of C, rated HF2, being the coating with less spalling and cracks in the vicinity of the indentation. The nanoindentation outcomes showed increased stiffness and hardness with higher carbon content of the films. Also, a twenty-fold hardness upgrade from the pure coating to the 24 at. % of C has

revealed that a limited carbon presence already augments this property fairly. The POD experiments, performed in humid air, disclose that NBR countersurfaces sliding against MoSeC have friction values of 0.56-0.87 for 25°C and 0.16-0.41 for 200°C. Meanwhile, sliding against steel countersurfaces manifests in much reduced values of 0.07 to 0.10 at 25°C and 0.06 to 0.08 at 200°C. Higher CoF for NBR is plausible as rubber is very soft hence the asperities of its surface deform to increase the area of contact and consequent friction. Lower CoF for high temperature tests, especially in higher at. % of C coatings, can be explained by the graphitization of amorphous C. This event reduces the shear strength of the carbon phase in the sliding. Focusing at the friction curves, the CoF drop, until a steady state regime is reached, was longer for NBR relative to steel; similar trend occurs for higher carbon content films relative to lower ones. Moreover, when sliding against steel, very high wear rates were observed in the pure $MoSe_2$ film, but no friction spikes were detected in its friction curves, likely meaning the Cr interlayer was not reached. No friction-wear proportionality existed, as checked by 3D optical profilometry. Nonetheless, the higher carbon content coatings displayed less wear and elevated CoF, probably because the high hardness retards the material loss. Also, the lowest absolute specific wear rates were for the 51 at. % of C film, which combines increased hardness, stiffness and compactness, thereby improving the wear resistance. A variable which correlates with the CoF, for 200°C experiments, is the wear track scar width. This is not valid for the 25°C tests, in which the scar width is constant at all carbon content films, thus empowering the chance for graphitization to be enlarging the scar. Combining the results from every experiment, the selection matrix in **Table B.1** chooses subjectively the 51 at. % of C film as the best performer.

For future works, more aims can be accomplished. First, an investigation on the scar after the POD test to discover the new chemical composition of the sliding region. Moreover, a laser patterning treatment could be introduced in the coatings, by crystallizing certain spots in the surface of the coating, to facilitate the reorientation mechanism and ameliorate the CoF from the initial sliding cycles. Finally, a practical cost-analysis to ascertain the economic viability of MoSeC in the tire molding industry could be executed.

BIBLIOGRAPHY

[1] Vuchkov, T., Yaqub, T. B., Evaristo, M. & Cavaleiro, A., (2020), “Synthesis, Microstructural, An Mechano-Tribological Properties Of Self-Lubricating W-S-C(H) Thin Films Deposited by Different RF Magnetron Sputtering Procedures”, Coatings 2020, 10, 272.

[2] Colas, G., Saulot, A., Regis, E. & Berthier, Y., (2015), “Investigation Of Crystalline And Amorphous MoS2 Based Coatings: Towards Developing New Coatings for Space Applications”, Wear, 330–331, 448–460.

[3] Yaqub, T. B., Vuchkov, T., Evaristo M. & Cavaleiro, A., (2019), “DCMS Mo-Se-C Solid Lubricant Coatings – Synthesis, Structural, Mechanical And Tribological Property Investigation”, Surface and Coatings Technology, 378.

[4] Polcar, T., Evaristo, M., Colaço, R., Sandu, C. S. & Cavaleiro, A., (2008), “Nanoscale Triboactivity: The Response Of Mo-Se-C Coatings To Sliding”, Acta Materialia, 56, 5101-5111.

[5] Yaqub, T. B., Vuchkov, T., Sanguino, P., Polcar, T. & Cavaleiro, A., (2020), “Comparative Study Of DC And RF Sputtered MoSe2 Coatings Containing Carbon—An Approach To Optimize Stoichiometry, Microstructure, Crystallinity And Hardness”, Coatings 2020, 10, 133.

[6] Sigeda, B., (2016), “The Effect of N Content On the Structure, Mechanical Properties And Tribological Behaviour Of TMD Coatings In Contact With Rubber”, Degree of Masters in Tribology Of Surface and Interfaces, Departamento de Engenharia Mecânica, Faculdade de Ciências e Tecnologia, Universidade de Coimbra, Coimbra.

[7] Kendall, D., (2008), “Mould Releases – An Overview”, Reinforced Plastics, 52(7), 32–34.

[8] Packham, D. E., (2002), “Mould Sticking, Fouling and Cleaning”, Rapra Review Reports, 150.

[9] Petrie, E. M., (2012), “Abhesion - The Science Of Non-Stick Surfaces”, Metal Finishing, 110(6), 28–31.

[10] Research, G., V., (2016), “Lubricants Market Analysis And Segment Forecasts To 2022”, Retrieved March 12, from: {"https:/www.grandviewresearch.com/industry-analysis/lubricants-market"}.

[11] Made, H., P., A., "How Tire Is Made - Material, History, Used, Processing, Parts, Components, Composition, Steps, Product", Retrieved March 12, 2020, from: {"http://www.madehow.com/Volume-1/Tire.html"}.

[12] Bandini, S., Colombo, E., Sartori, F. & Vizzari, G. (2004), "Case Based Reasoning And Production Process Design: The Case Of P-Truck Curing, 3155, 504-517.

[13] Kpzen, (2016), "Small cracks on my ~ 1 year old tires. Is this normal?", Retrieved March 6, 2020, from: {"https://www.team-bhp.com/forum/tyre-alloy-wheel-section/177212-small-cracks-my-1-year-old-tyres-normal-3.html"}.

[14] Arjit, R., (2015), "Why Do All Tires Have Extrusions On Its Surface?", Retrieved March 8, 2020, from: {"https://www.quora.com/Why-do-all-tyres-have-extrusions-on-its-surface"}.

[15] Kato, K., (2014), "Classification of Wear Mechanism Models", Wear: Materials, Mechanisms and Practice, Stachowiak, G., W., Ed., 9-18.

[16] Ganapathi, A., (2017), "Tribology", Retrieved March 13, 2020, from: {"https://pt.slideshare.net/machamadaganapathi/tribology-75658698"}.

[17] Mofidi, M., (2007), "Tribology of Elastomers", Licentiate Thesis, Department of Applied Physics and Mechanical Engineering, Division of Machine Elements, Luleå University of Technology.

[18] Persson, B. N. J., (2001), "Theory Of Rubber Friction And Contact Mechanics", The Journal of Chemical Physics, 115, 3840.

[19] Gal, A. L. & Klueppel, M. (2008), "Investigation And Modelling Of Rubber Stationary Friction On Rough Surfaces", Journal of Physics: Condensed Matter, 20, 015007.

[20] Hadjittofis, E., Das. S, Zhang, G. & Heng, J., (2017), "Developing Solid Oral Dosage Forms: Pharmaceutical Theory And Practice"; Elsevier 2º Ed., 225-252.

[21] Leach, A., (2006), "Comprehensive Medicinal Chemistry II", Elsevier, 4, 87-118.

[22] Singh, A., (2016), "Engineered Nanoparticles", Elsevier, 19-76.

[23] Adair, J., Suvaci, E. & Sindel, J., (2001), "Encyclopedia Of Materials: Science And Technology", Elsevier, 1-10.

[24] International, M., C., "Permanent Mold Release – Enhanced Efficiency In Tire Production", Retrieved March 25, 2020, from: {"https://www.muench-chemie.com/en/tire-production-tire-moulds.html"}.

[25] Koçak, A., (2018), “Materials Science And Engineering #Thin Film Preparation, Particle Size And Thickness Analysis Experimental Report”, Technical Report, Anadolu University, 2.

[26] Cavaleiro, A. & Vieira. M.T., (1995) “Engenharia De Superfícies E Degradação E Protecção De Superfícies”, Textos de Apoio à Lecionação das Disciplinas de Mestrado: Engenharia de Superfícies (Mestrado em Engenharia Mecânica, FCTUC) e Degradação e Protecção de Superfícies (Mestrado Nacional em Engenharia dos Materiais), Departamento de Engenharia Mecânica, Universidade de Coimbra.

[27] Bondarev, A. V., Kiryukhantsev-Korneev, P. V., Sheveyko, A. N. & Shtansky, D. V. (2015), “Structure, Tribological And Electrochemical Properties Of Low Friction TiAlSiCN/MoSeC Coatings”, Applied Surface Science, 327, 253–261.

[28] Ahmad, I., Khan, S. A., Idrees, M., Haneef, M., Shahid, I., Din, H. U., Khan, S. A. & Amin, B. (2018), “Influence Of Strain On Specific Features Of MoX2 (X = S, Se, Te) Monolayers”, Physica B: Condensed Matter, 545, 113–118.

[29] Guan, X., Zhu, G., Wei, X. & Cao, J. (2019), “Tuning The Electronic Properties Of Monolayer MoS2, MoSe2 And MoSSe By Applying Z-Axial Strain”, Chemical Physics Letters, 730, 191–197.

[30] Gustavsson, F., Jacobson, S., Cavaleiro, A. & Polcar, T., (2013), “Frictional Behavior of Self-Adaptive Nanostructural Mo-Se-C Coatings In Different Sliding Conditions”, Wear, 303(1–2), 286–296.

[31] Polcar, T., Evaristo, M. & Cavaleiro, A. (2009), “Comparative Study Of The Tribological Behavior Of Self-Lubricating W-S-C And Mo-Se-C Sputtered Coatings”, Wear, 266(3–4), 388–392.

[32] Polcar, T., Evaristo, M., Stueber, M., & Cavaleiro, A. (2007), “Synthesis And Structural Properties Of Mo-Se-C Sputtered Coatings”, Surface and Coatings Technology, 202(11), 2418–2422.

[33] Grigoriev, S. N., Fominski, V. Y., Romanov, R. I., & Gnedovets, A. G. (2014), “Tribological Properties Of Gradient Mo-Se-Ni-C Thin Films Obtained By Pulsed Laser Deposition In Standard And Shadow Mask Configurations”, Thin Solid Films, 556, 35–43.

[34] Raju, G. (2015), “Tribological Study Of TMD Coatings For Rubber Applications”, Degree Of Masters In Materials Engineering, Departamento de Engenharia Mecânica, Faculdade de Ciências e Tecnologia, Universidade de Coimbra, Coimbra.

[35] Bajpai, P., (2017), “Pulp And Paper Industry”, Elsevier, 105-212.

[36] Polcar, T., (2009) “Self-Lubricating Nanostructured Coatings Based On Transition Metal Dichalcogenides Alloyed With Carbon”, Habilitation Thesis, Czech Technical University, Prague.

[37] Zhu, S., Cheng, J., Qiao, Z. & Yang, J., (2019), “High Temperature Solid-Lubricating Materials: A Review”, Tribology International, 133, 206-223.

[38] Joerg, T., Cordill, M. J., Franz, R., Glushko, O., Winkler, J. & Mitterer, C. (2016), “The Eletro-Mechanical Behavior Of Sputter-Deposited Mo Thin Films On Flexible Substrates”, Thin Solid Films, 606, 45-50.

[39] Zhao, X., Cai, W., Yang, Y., Song, X., Neale, Z., Wang, H. E., Sui, J. & Cao, G. (2018), “MoSe2 Nanosheets Perpendicularly Grown On Graphene With Mo–C Bonding For Sodium-Ion Capacitors”, Nano Energy, 47, 224–234.

[40] Mashmool, A., Saeidi, P., Yalameha, S., & Nourbakhsh, Z. (2020), “First Principles Calculations Of Structural, Electronic And Optical Properties MoX2 (X = S, Se) Metal Dichalcogenides And Their Nano-Layers”, Journal of Magnetism and Magnetic Materials, 503.

[41] Ji, W., Chu, X., Zhang, S., Wang, D., & Ma, Y. (2018), “Active Basal Plane In ZT-Phased MX2 (M = Mo, W; X = S, Se, Te) Catalysts For The Hydrogen Evolution Reaction: A Theoretical Study”, International Journal of Hydrogen Energy, 43(42), 19432–19437.

[42] Nossa, A. & Cavaleiro, A., (2001) “The Influence Of The Addition Of C And N On The Wear Behaviour Of W-S-C/N Coatings”, Surface and Coatings Technology, 142:984–991.

[43] Wasa, K., Kitabatake, M. & Adachi, H., (2013), “Thin Film Materials Technology”, Norwich, NY: William Andrew Pub.

[44] Adachi, H., Wasa, K., Kanno, I. & Kotera, H., (2012), “Handbook Of Sputter Deposition Technology”, Waltham, MA: William Andrew.

[45] Seshan, K., (2002), “Handbook Of Thin Film Deposition”, Waltham [Mass.]: William Andrew.

[46] Mattox, D.M., (2010), “Handbook Of Physical Vapor Deposition (PVD) Processing”, Elsevier 2º Ed.

[47] Oura, K., Katayama, M., Zotov, A.V., Lifshits, V.G. & Saranin, A.A., (2003), “Surface Science”, Surface Science, Berlin, Heidelberg: Springer Berlin Heidelberg.

[48] Doi, I., "Processos de Filmes Finos", Retrieved March 27, 2020, from: {"https://slideplayer.com.br/slide/367509/"}.

[49] Jameel, D. A. (2015), "Thin Film Deposition Processes", International Journal of Modern Physics and Applications, 1(4), 193-199.

[50] Ganga, S., "Chapter 2: Thin Film Deposition", Retrieved March 30, 2020, from: {"https://shodhganga.inflibnet.ac.in/bitstream/10603/79579/12/12_chapter%202.pdf"}.

[51] Madhu, (2011), "Difference Between PVD And CVD", Retrieved March 28, 2020, from: {"https://www.differencebetween.com/difference-between-pvd-and-vs-cvd/"}.

[52] Bellardita, M., Paola, A., D., Yurdakai, S. & Palmisano, L., (2019), "Preparation Of Catalysts And Photocatalysts Used For Similar Processes", Heterogeneous Photocatalysis, 25-56.

[53] Swann, S. (1988), "Magnetron Sputtering", Physics in Technology, 19(2).

[54] Gwyddion, (2020), "Gwyddion", Retrieved June 5, from: {"http://gwyddion.net/"}.

[55] Maggio, M., (2017), "Carbon-Based Nanomaterials", Degree of Doctor Thesis in Chemistry, Department of Chemistry and Biology, University of Salerno, Salerno.

[56] Muratore, C. & Voevodin, A.A., (2009), "Control Of Molybdenum Disulfide Basal Plane Orientation During Coating Growth In Pulsed Magnetron Sputtering Discharges", Thin Solid Films, 517, 5605–5610.

[57] Vaidya, A. & Pathak, K., (2019), "Mechanical Stability Of Dental Materials", Applications of Nanocomposite Materials in Dentistry, 285-305.

[58] Kuiry, S., (2012), "Advanced Scratch Testing For Evaluation Of Coatings", Retrieved May 7, 2020, from: {"https://www.bruker.com/fileadmin/user_upload/8-PDF-Docs/SurfaceAnalysis/TMT/Webinars/Advanced-Scratch-Testing-for-Evaluation-of-Coatings-Slides.pdf"}.

[59] Shamshiri, M., Manaia, A., Vuchkov, T., Carvalho, A., Gaspar, G., Fernandes, M., Dolatabadi, S., H., Costa, F. & Cavaleiro, A., (2020), "Influence Of Laser Structural Patterning On The Tribological Performance Of C-alloyed W-S Coatings", Surface and Coatings Technology, 394.

[60] Greenwood, J., A. & Williamson, J., B., P., P., (1966), "Contact Of Nominally Flat Surfaces", Proceedings of the Royal Society A Mathematical Physical and Engineering Sciences, 295, 300-319.

[61] Henry, D., Goodge, J., (2016), "Wavelength Dispersive X-Ray Spectroscopy (WDS)", Retrieved June 20, from: {"https://serc.carleton.edu/research_education/geochemsheets/wds.html"}.

[62] Bradbury, S., Joy, D., C. & Ford, B., J., (2020), "Scanning Electron Microscope", Retrieved June 22, from: {"https://www.britannica.com/technology/scanning-electron-microscope"}.

[63] Swapp, S., (2017), "Scanning Electron Microscopy (SEM)", Retrieved June 22, from: {https://serc.carleton.edu/research_education/geochemsheets/techniques/SEM.html}.

[64] XOS, (2020), "X-Ray Diffraction", Retrieved June 25, from: {"https://www.xos.com/XRD"}.

[65] Sima, F., Ristoscu, C., Duta, L., Gallet, O., Anselme, K. & Mihailescu, I., N., (2016), "X-Ray Diffraction", Laser Surface Modification of Biomaterials, 77-125.

[66] Salisu, N., Hussein, M., Z., Zainal, Z. & Yusof, N., A., (2018), "Potential Valorization Of By-Product Materials From Oil Palm: A Review Of Alternative And Sustainable Carbon Sources For Carbon-Based Nanomaterials Synthesis", Bioresources, 14(1).

[67] Xi, Y., Bai, Y., Gao, K. & Pang, X., (2018), "In-Situ Stress Gradient Evolution Texture Dependent Fracture Of Brittle Ceramic Thin Films Under External Load", Ceramics International, 44(7).

[68] Testing, N., H., (2016), "Rockwell Hardness Testing", Retrieved June 30, from: {"https://www.hardnesstesters.com/test-types/rockwell-hardness-testing"}.

[69] Yovanovich, M., M., (2006), "Micro And Macro Hardness Measurements, Correlations And Contact Models", Aerospace Science Meeting and Exhibition, Department of Mechanical Engineering, University of Waterloo, Waterloo.

[70] Instruments, N., S., (2020), "Nanoindentation", Retrieved June 30, from: {"https://www.nanoscience.com/techniques/nanoindentation/"}.

[71] Shanks, R., A., (2014), "Tapping Mode – An Overview", Nanostructure Polymer Blends, 15-31.

[72] Magonov, S., (2001), "Visualization Of Polymers At Surfaces And Interfaces With Atomic Force Microscopy", Handbook of Surfaces and Interfaces of Materials, 2, 393-430.

[73] Materials, A., (2019), "Types Of Scanning Probe Microscopy", Proceeding on the International Conference of Advanced Materials, Rome, Italy, May 22-23.

[74] Tribonet, (2019), “Pin On Disk Test”, Retrieved July 5, from: {"https://www.tribonet.org/wiki/pin-on-disk-test/"}.

[75] Azad, K., Rasul, M., G., Khan, M., M., K. & Sharma, S., C., (2019), “Ecofuel And Its Compatibility With Different Automotive Metals To Assess Diesel Engine Durability”, Woodhead Publishing Series in Energy, 337-351.

[76] Alicona, B., (2020), “Dimensional Accuracy & Surface Finish Measurement”, Retrieved July 7, from: {"https://www.alicona.com/en/products/infinitefocus/"}.

ANNEX A: BRIEF FUNDAMENTAL THEORY OF THE CHARACTERIZATION TECHNIQUES

WDS (for Chemical Composition): When an electron beam of enough energy hits a sample, X-rays are generated on the atoms of the latter. These rays are focused by a lens, from the sample to an analytical crystal, at a specific angle. When the X-ray encounters the analytical crystal at this angle, only the X-rays satisfying the Bragg's law for the specific chemical element of the crystal are focused to a detector, in a ray with the correspondent single wavelength of that element. After, the detector only converts the electrical signal generated to a certain abundance of the equivalent chemical element. Usually, multiple spectrometers with a suite of analytical crystals of different chemical elements are present in the same WDS instrument, so that the spectrometers can reach all elemental wavelengths of interest. A scheme of the underlying mechanism of WDS is illustrated in **Figure A.1** [61].

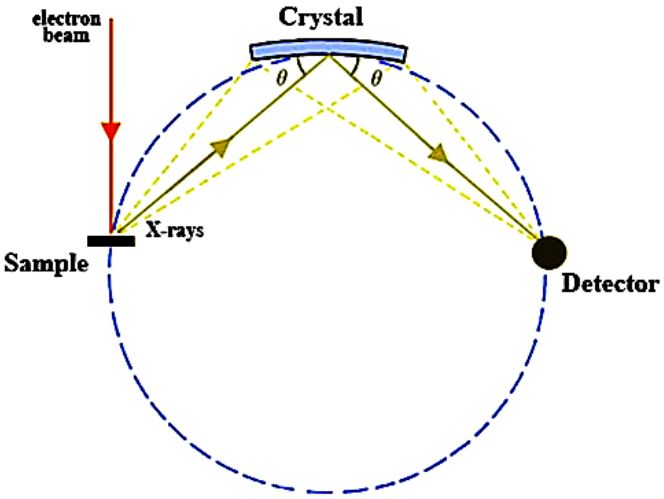

Figure A.1. Illustration of the WDS fundamental principle – adapted from [61].

SEM (for Thickness and Surface Morphology): SEM utilizes an electron gun to shoot a beam of relatively low energy electrons and a magnetic lens to focus these and scan the sample in a regular pattern. This is shown in **Figure A.2**. The action of the electron beam on the specimen

causes the emission of low-energy secondary electrons, from the surface of the specimen, and high-energy backscattered electrons, from deeper in the coating. These emitted electrons are then detected in a secondary electron detector and a backscattered electron detector, respectively, and the signals that derive from this electron-sample interaction, reveal information about the sample, such as the thickness and topology of the coating, which can be visualized in a generated 2-dimensional image of the scanning zone [62, 63].

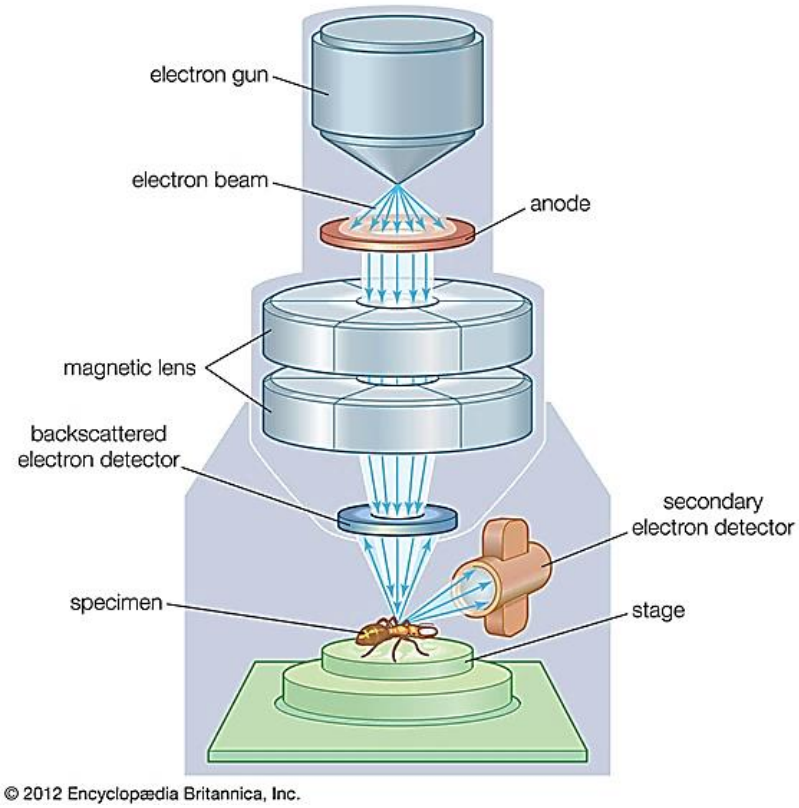

Figure A.2. Basic equipment and underlying mechanism in SEM – adapted from [62].

GIXRD (for Crystal Structure): Once an incident beam of monochromatic X-rays hits a sample, the X-rays are scattered at multiple angles through lattice interatomic spaces within the sample. Then, if at certain angles, the structure of the crystals is more crystalline, the scattered waves increase, which leads to constructive interferences of multiple waves. Thus, at these specific angles, which can be determined through the known Bragg's law, peak intensities are observed in the diffracted X-rays detector. If the experimental angle of the detector is systematically changed within a certain range, all the correspondent peaks can be detected. **Figure A.3** illustrates the principle of XRD at the atomic scale, including the formulation of the Bragg's law, whereas **Figure**

A.4 shows the typical configuration of the utilized XRD technique, GIXRD. In this configuration, the beam source is fixed at a constant grazing incidence angle and the detector rotates 2θ, given that θ is the incident beam angle relative to each of the sample diffraction planes. Usually, GIXRD configuration is introduced instead of typical XRD when thin films are analyzed. In typical XRD weak signals arise from the coating and more intense ones from the substrate. So, GIXRD is inserted to diminish the depth at which scattering occurs on the coating [64, 65].

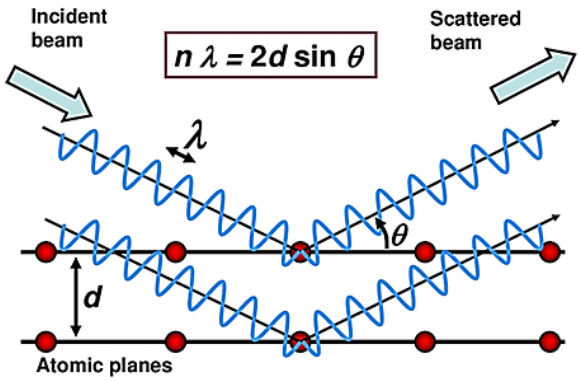

Figure A.3. X-ray diffraction explained concept – adapted from [66].

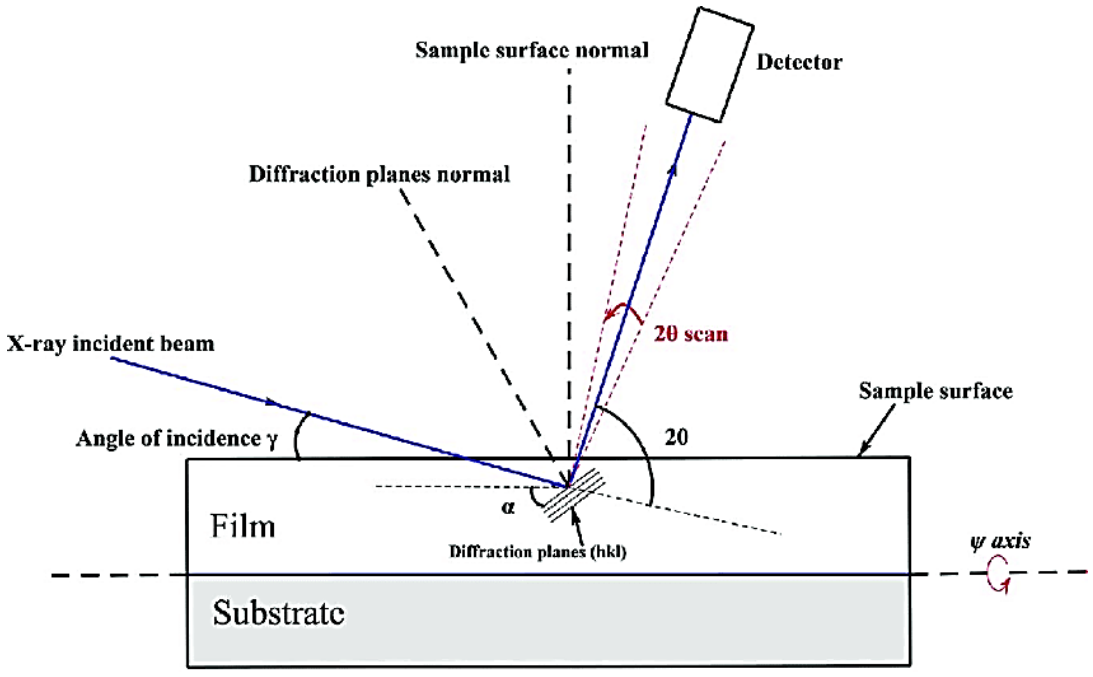

$$\alpha = \theta - \gamma$$

Figure A.4. GIXRD configuration – adapted from [67].

Scratch Test (for Adhesion): Scratch test is an efficient method to determine the adhesion strength of a coating to a substrate. For this, the surface of a coating is penetrated by an indenter, which scratches the coating at a constant sliding velocity. If, as in this research, the scratch test constitutes a progressive load one, the indenter is drawn across the specimen surface with a linearly increasing load applied, presenting normal and tangential components. A scheme of the Scratch test can be visualized in **Figure A.5**. The smallest loads at which a failure event on the substrate-coating interface occurs are named critical loads. The events can be identified by visual inspection through optical microscopy or by acoustic emission, via sudden increases in signal at the critical loads. Then, resorting to an optical microscope, the location of the event is probed [58].

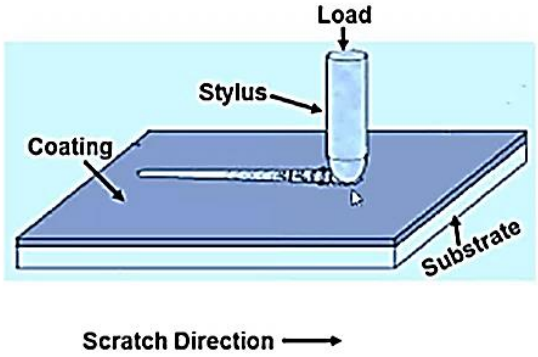

Figure A.5. Scratch adhesion test representative scheme – adapted from [58].

Rockwell C Indentation (for Adhesion): Rockwell C is a refined estimator to quantify the resistance of a material to a permanent shape change, when subjected to a constant compressive force. In this test, an initial minor load establishes the reference level of indentation and is able to avoid the surface grinding effects of the sample. Then, a major load is added, and a total load is achieved. Finally, the major load is removed and only the minor load stays applied. This way, the Rockwell C experiment determines the hardness of a material by measuring the penetration difference between after and before the major load was introduced. This is represented in **Figure A.6**. The Rockwell C Indentation test assumes vast importance as it displays a reasonable approximation to other mechanical properties, such as strength or ductility of a material, or even to the adhesion strength of a coating. Thus, it is a simple and fast method to control the quality of a material. In this research, Rockwell C Indentation tests allowed to understand the level of adhesion of the coatings to the substrates [68, 69].

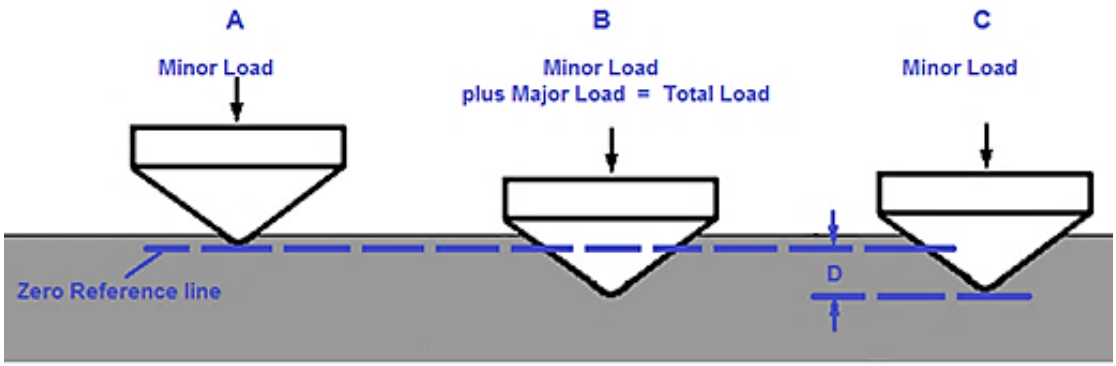

Figure A.6. Rockwell C Indentation working principle – adapted from [68].

Nanoindentation (for Hardness and Mechanical Properties): Nanoindentation is a technique utilized to evaluate the hardness and other mechanical properties of a coating, at depths of only about 10 % of the coatings thickness, so that minimal effect from the substrate on the measurement is verified. The Nanoindentation test provides several results. These are analyzed resorting to load vs displacement curves. Whereas the loading curve gives information on both elastic and plastic domains, the unloading curve allows to have data on the elastic recovery. The two most important mechanical properties extracted from Nanoindentation are the reduced Young's modulus, E, and the hardness, H, which can be visualized in **Figure A.7**.

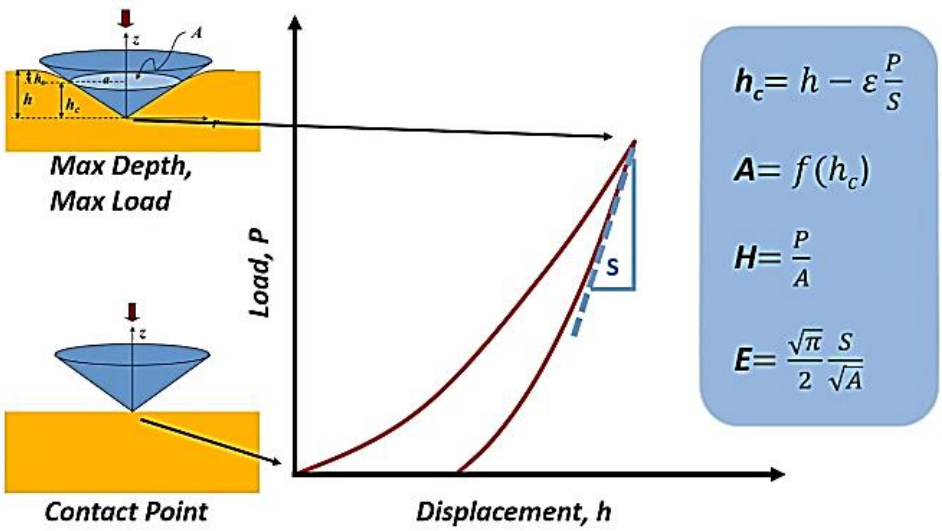

Figure A.7. Nanoindentation characteristic test and load vs displacement curves – adapted from [70].

Atomic Force Microscopy (for Surface Topology): in AFM tapping mode, a cantilever tip interacts with a specimen by oscillating vertically above the latter. In **Figure A.8** the laser focused beam produces a deflection of the cantilever tip, which is then measured and converted to an electrical signal, via a photodiode. In AFM tapping mode, a piezoelectric holder (or even piezoelectric cantilever) permits an oscillation mode of the tip, at certain frequencies, not to damage the surface, as the tip barely touches it.

This technique relies on van der Waals interatomic forces. Dependent of the distance between probe and sample surface, the van der Waals force assumes different values. Because of these force variations, the tip-sample interactions should also vary in amplitude. Thus, during scanning, the amplitude is maintained at a constant level by electronics, by adjusting the relative position of the tip with respect to the sample. It is the damping of amplitude due to each tip-sample contact that is utilized for surface profiling, as the adjustments of the z-position are represented in a height image. AFM can evaluate both surface morphology and topography and may also allow an approximation for the average rugosity of a sample [71, 72].

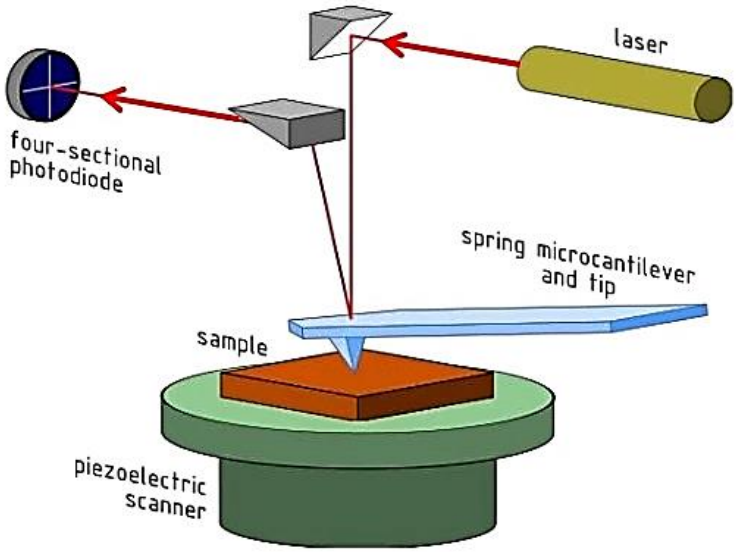

Figure A.8. AFM principal components representation – adapted from [73].

Pin-On-Disk (for Friction Curves): pin-on-disk, represented in **Figure A.9** is an experiment which requires a stationary pin to be forced, by a given perpendicular load, against a rotating disk. The pin can assume different shapes, such as spherical or cylindrical. A spherical ball was utilized, in the ambit of this research. During a certain number of sliding cycles, the relative

linear velocity between the disk and pin is kept constant on the friction track radius and the normal applied load is also unchanged. Hence, the friction force is continuously monitored via sensor, and the friction curve is plotted, representing the CoF vs the number of cycles or time already spent since the start of the test. At the beginning of the test a running-in stage appears in the friction curves, in which the measured coefficient of friction is a little higher and unstable. However, due to the occurrence of structural changes on the coating near surface area, the CoF assessed value tends to drop until it reaches a certain stability. In this case, the system achieves a steady state regime, whose COF is usually reported for tribological analysis and comparison purposes [74, 75].

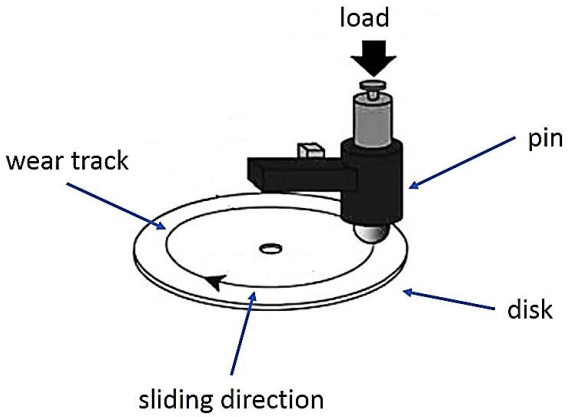

Figure A.9. Pin-on-disk fundamental mechanism – adapted from [74].

3D Optical Profilometer (for Wear Rate): 3D optical profilometer is an apparatus able to probe topographical data from a sample surface. For instance, it can provide a 3D scan of a surface and utilize it to know the worn area in a certain cross-sectional profile of a film, after a POD experiment. The profilometer device is composed by a beam splitting mirror onto which a light source is focused and goes through, and an objective centers it to the specimen. Depending on the sample topography the light backscatters into different directions. If the surface has diffused reflective characteristics, the light is reflected more to certain directions. So, when rays are backscattered to the objective lens after hitting the sample, they are bundled in the optics and measured by a light sensitive sensor. Due to the small depth field of the optics, sharp images are only extrapolated for low surface heights. Therefore, the optics must be moved vertically along the optical axis so that it focuses each region of depth from the sample. Then, a software converts the acquired data to a surface image, via comparing the different vertical changes that allow distinct focus depths [76].

APPENDIX A: CHOICE OF $MOSE_2$ AS TMD AND OF AMORPHOUS CARBON AS MATRIX

Table A.1. Explanation of the choice of $MoSe_2$ as the utilized TMD.

	$MoSe_2$ Characteristics and their Implications
Interest	Low Research Volume
	Potential Solid Lubricant
Electrical and Optical	Semiconductor
	Narrower Bandgap than Other TMDs => Better Electrical Conductor
	Direct Bandgap (at less than 1 % compressive strain) => Good Light Absorption
	Ultra-high Activity as HER Electro Catalyst
	Mo-C Bonds => Fast Charge Transfer
Mechanical and Tribological	Ductile => Sustain High Deformations Before Fracture
	Elastically Anisotropic
	Mechanically Stable
	Lower Shear Modulus than Other TMDs and Larger Interplanar Distances => Easier Shearing
	Superior Oxidation Resistance compared to Most TMDs => Only triggers Higher Rates of Corrosion at Temperatures > 450°C
	High Frictional Stability => Favorable Tribological Results at Temperatures < 300°C in Humid Air, Dry Nitrogen and Vacuum
	Very Low Friction in Humid Air (Uncommon for TMDs) => Low CoF and Wear Resistant

Table A.2. Explanation of the amorphous carbon choice as the utilized matrix.

Amorphous Carbon Advantages as a Matrix
Improved Hardness
Improved Wear Resistance
Higher Compactness => Less Oxygen Bonds => Better Corrosion Resistance
Amorphousness => Semiconductor Behavior + Higher Compactness

APPENDIX B: SELECTION MATRIX OF COATING WITH BEST MECHANICO-TRIBOLOGICAL BEHAVIOR

Table B.1. Matrix utilized to evaluate and compare the MoSeC coatings (pure $MoSe_2$, 24 at. % of C, 33 at. % of C, 51 at. % of C, 60 at. % of C) in terms of the mechanical properties and tribological performance.

		Rating (0-1)				
Properties	**Weigthing (0-1)**	**Pure $MoSe_2$**	**24 % at. C**	**33 % at. C**	**51 % at. C**	**60 % at. C**
Se/Mo Ratio	0.16 (16/100)	1	1	0.85	0.7	0.5
Compactness	0.14 (14/100)	0.4	0.5	0.6	1	1
Adhesion Strength	0.18 (18/100)	0	0.4	0.7	1	1
Hardness	0.16 (16/100)	0.1	0.6	0.65	0.95	1
CoF	0.18 (18/100)	0.85	0.95	1	0.75	0.75
Specific Wear Rate	0.18 (18/100)	0.2	0.65	0.5	1	0.95
	1	0.42	0.69	0.72	**0.90**	0.87

The adhesion strength, CoF and specific wear rate have taken the maximum weighting since they are crucial and directly related with the tribological and mechanical performance of the film. A reasonable influence on the behavior of the coating have the Se/Mo ratio (leading to higher lubricity and self-adaptive mechanism) and the hardness (providing better resistance to plastic deformation of the coating, that could eventually turn into several failures during sliding). On the other hand, and despite being an important property too, the compactness is related to the film resistance to wear in an indirect manner (since it increases the environmental resistance), not being the major factor influencing the behavior of the coating friction-wise. Surely, after some time from the start of the relative motion between two surfaces, the latter property is going to be crucial to define the film ability to maintain the adequate chemical composition in the sliding region. But it is not a quintessential property in order to provide low friction from the initial sliding cycles.

As for the weighting, the values written in the table for the compactness, adhesion strength and hardness were assumed to be more beneficial if higher. CoF and specific wear rate were assumed to be more beneficial if lower. Also, an assumption was taken that Se/Mo ratio is very good (weighting of 1) whenever it is over the value of 1.75 and decreases proportionally with a decrease in Se/Mo values under that. Other properties than the above were not considered since the current knowledge on the topic still lacks certainty about what is the optimal trend for those specific properties, e.g. the higher the value of the property the better.